Atmospheric
Chemistry
and Physics
Discussions

Modeling and evaluation of the global sea-salt aerosol distribution: sensitivity to emission schemes and resolution effects at coastal/orographic sites

M. Spada[1], O. Jorba[1], C. Perez[2,3], Z. Janjic[4], and J. M. Baldasano[1,5]

[1]Barcelona Supercomputing Center – Centro Nacional de Supercomputación, Barcelona, Spain
[2]NASA Goddard Institute for Space Studies, New York, USA
[3]Department of Applied Physics and Applied Math, Columbia University, New York, USA
[4]National Centers for Environmental Prediction, College Park, Maryland, USA
[5]Universitat Politècnica de Catalunya, Barcelona, Spain

Abstract

We investigate two of the major sources of uncertainty in the model estimation of the global distribution of sea-salt aerosol, i.e. the sensitivity to the emission parameterization and the influence of model resolution in coastal regions characterized by complex topography and/or steep orographic barriers where some observation sites are located. We evaluate a new sea-salt aerosol lifecycle module implemented within the online chemical transport model NMMB/BSC-CTM. Because of its multiscale core, the model is able to cover a wide range of scales. Global simulations using four state-of-the-art sea-salt emission schemes are evaluated against monthly-averaged aerosol optical depth (AOD) from selected AERONET Sun photometers, surface concentration measurements from the University of Miami's Ocean Aerosol Network and measurements from two NOAA/PMEL cruises (AEROINDOEX and ACE1). The model results are highly sensitive to the introduction of SST-dependent emissions and to the accounting of spume particles production. Depending on emission scheme, annual emissions range from 4312.9 Tg to 8979.7 Tg in the 2006. Sea-salt lifetime varies between 7.7 h and 12.0 h and the annual mean column mass load is between 5.9 Tg and 7.9 Tg. Observed coarse AOD monthly averages are reproduced with an overall correlation around 0.8 (a correlation of 0.6 is produced when applying the SST dependent scheme). Although monthly-averaged surface concentrations are overall in good agreement with the observations, there is a subset of coastal sites surrounded by complex topography where the global model overestimates by a factor of 2 or more. Using regional high-resolution simulations, we show that these large errors are mostly due to the global model's inability to capture local scale effects. In New Zeland, the increase in resolution produces a significant decrease of surface concentrations (up to 40 %) – due to changes in the wind circulation and precipitation driven by the orographic barrier – which is in close agreement with surface concentration monthly climatologies measured by University of Miami stations in the region (Baring Head, Chatam Island and Inverncargill). The observed climatological precipitation in this area is well

reproduced by the model at high resolution, while it is strongly underestimated when employing coarser scales. Our results outline that caution may be taken when evaluating and/or constraining coarse global sea-salt simulations with observations around coastal/orographic sites.

1 Introduction

Sea-salt is one of the most abundant aerosol species at global scale. It perturbs radiative fluxes directly by interacting with shortwave and longwave radiation, and indirectly by acting as cloud condensation nuclei (CCN) and thus altering marine cloud brightness and lifetime. It also influences heterogeneous chemistry mainly over coastal areas (Lewis and Schwartz, 2004). The major uncertainties in the sea-salt life cycle are emission (Textor et al., 2006; de Leeuw et al., 2011), water-uptake (Textor et al., 2006), and deposition (Textor et al., 2007); the chemical composition can also play an important role in the sea-salt direct and indirect radiative effects (Tsigaridis et al., 2013). Lewis and Schwartz (2004) estimate the total sea-salt emission to vary from $0.3\,\mathrm{Tg\,yr^{-1}}$ to $30\,\mathrm{Tg\,yr^{-1}}$ and estimates from models involved in the AEROCOM project range from $3\,\mathrm{Tg\,yr^{-1}}$ to $18\,\mathrm{Tg\,yr^{-1}}$ for year 2000 (Textor et al., 2006). These uncertainties may lead to differences of a factor of 2 or more in the simulated monthly-averaged concentrations among different models, and between simulated and observed concentrations (Textor et al., 2006). The lack of comprehensive measurement datasets makes difficult the evaluation efforts and the improvement of sea-salt models and related parameterizations, e.g., for a given region and a given time period, only a few coincident measurements of surface concentration, aerosol optical depth (AOD), and particle-size distribution are available. Also just a few emission and deposition flux estimates at specific sites and temporal intervals are found in literature. Additional difficulties arise from biases in satellite retrievals particularly in the most important sea-salt production regions (e.g. Jaeglé et al., 2011).

Several approaches are commonly used for the parameterization of the sea-salt emission process, from semi-empirical combinations of whitecap factorization and concentration measurements (Monahan et al., 1986; Smith et al., 1993; Smith and Harrison, 1998; Andreas, 1998; Hoppel et al., 2002; Gong, 2003; Petelski et al., 2005; Mårtensson et al., 2003; Clarke et al., 2006; Caffrey et al., 2006; Jaeglé et al., 2011; Fan and Toon, 2011), to empirical methods (such as the use of concentration vertical profiles from aircraft observations by Reid et al., 2001). Parameterizations of the sea-salt emission fluxes may account for different production mechanisms (bubble bursting, spume cutting), which may depend on different meteorological parameters. The most used parameter is wind speed at $10\,\mathrm{m}$ (U_{10}) but there have also been attempts to include dependencies upon sea surface temperature (SST), wave height, increasing/decreasing wind, salinity and other parameters. Exhaustive reviews of these efforts and their performance can be found in Lewis and Schwartz (2004), O'Dowd and de Leeuw (2007), and de Leeuw et al. (2011). The above-mentioned parameterizations are assumed for the open ocean. Production in the surf-zone represents an additional open issue (de Leeuw et al., 2000).

The high hygroscopicity of sea-salt requires water uptake schemes which range from the use of prescribed growth factors (Chin et al., 2002) or equations (Gerber, 1985; Ghan et al., 2001) to explicit calculations of the condensed aerosol water (Vignati et al., 2004). However, their performance is hard to assess and it remains an open topic for aerosol modeling (Textor et al., 2006).

Another source of uncertainty is given by the spatio-temporal scales involved in the sea-salt lifecycle. Even if the sea-salt parameterizations can be formulated independently from the model scales, they are driven by meteorological parameters which are affected by scaling effects particularly over coastal areas where some measurement stations are located.

In this contribution, we investigate the uncertainties associated with sea-salt emission schemes and the effects taking place in regions characterized by complex topography and/or steep orography. We use a new sea-salt module implemented within the

online multiscale NMMB/BSC Chemical Transport Model (NMMB/BCS-CTM) (Pérez et al., 2011; Haustein et al., 2012; Jorba et al., 2012), developed at the Barcelona Supercomputing Center in collaboration with NOAA/National Centers for Environmental Prediction (NCEP) and the NASA Goddard Institute for Space Studies. Its multiscale meteorological core, the Non-hydrostatic Multiscale Model NMMB (Janjic, 2005; Janjic and Black, 2007; Janjic et al., 2011; Janjic and Gall, 2012) allows to bridge the gap between global to regional and local scales. This feature is only found in few other state-of-the-art aerosol models, such as the GEM-AQ/EC model (Gong et al., 2012).

In Sects. 2 and 3 we present the modeling system along with the details of the sea-salt module development. We implement four emission parameterizations following the whitecap approach, in order to investigate this major source of uncertainty. Particular attention is given to the description of spume particles production and to the dependence of emissions on SST. In Sect. 4 we present the observational datasets used for the evaluation of global simulations. Global scale results are shown in Sect. 5.1. Evaluation is performed against cruise data from the NOAA/PMEL Laboratory, sea-salt concentration monthly climatologies from the University of Miami Ocean Aerosol Network and monthly-averaged measurements from distributed AERONET Sun photometers. In Sect. 5.2, we focus our attention on a regional domain covering the New Zealand region at high resolution ($0.1° × 0.1°$). We investigate the influence of the model resolution on wind circulation, precipitation, and the orographic gradients of the Southern Alps affecting the sea-salt aerosol concentration and annual trend.

2 Modeling background

The NMMB/BSC-CTM is a fully on-line chemical transport model under development at the Barcelona Supercomputing Center, coupling the atmospheric equations of NMMB with the gas-phase and aerosol continuity equations of BSC-CTM. At the present stage of development aerosol species included in the model are dust and sea-salt. The implementation and evaluation of other global-relevant aerosols is underway. Details on

Full Screen / Esc

Printer-friendly Version

Interactive Discussion

the dust aerosol module and gas-phase module can be found in Pérez et al. (2011) and Jorba et al. (2012), respectively. According to the features of its meteorological core, the Non-hydrostatic Multiscale Model (NMMB), the coupled model is intended for short- and medium-range forecasting for a wide range of spatial scales, from global to regional domains, as well as for climate studies (http://www.bsc.es/earth-sciences/ mineral-dust/nmmbbsc-dust-forecast). Due to its fully online coupling, several feedback processes among gases, aerosol particles and radiation are taken into account by the model. In particular, the direct radiative effect of aerosols is considered, while indirect effects are neglected at present time. The on-line coupling of aerosol optical properties and gas-phase photolysis reactions is also under development.

2.1 The NCEP non-hydrostatic multiscale model (NMMB)

The NMMB is the meteorological core of the modeling system allowing simulations of scales ranging from global to large eddy simulations (LES) in global and regional domains. The regional NMMB is used at NCEP as the regional North American Mesoscale (NAM) model since October 2011. The global model is formulated on the latitude-longitude grid, by applying conservative polar boundary conditions and polar filtering slowing down the tendencies of basic dynamical variables (Janjic, 2009; Janjic and Gall, 2012). Rotated latitude-longitude grids are employed for regional simulations in order to obtain more uniform grid distances. In both cases, the horizontal discretization is performed on the Arakawa B-grid. In the vertical, the general hybrid sigma-pressure coordinate (Simmons and Burridge, 1981) is used, by employing the Lorenz staggering. The "isotropic" horizontal finite volume differencing technique assures the conservation of a number of dynamical and quadratic quantities (among these, energy and enstrophy). More details about the numerical schemes in NMMB can be found in Janjic (1977, 1979, 1984, 2003) and in Janjic et al. (2001, 2011).

A variety of physical schemes are implemented in the model. A list of these parameterizations and respective references are presented in Pérez et al. (2011) and details can be found in Janjic (1990, 1994, 1996, 2001). For our purposes, we shortly

recall the parameterizations involved in the coupling of NMMB with the sea-salt module, i.e. the surface layer, grid scale cloud microphysics, convective adjustment and precipitation, and radiation scheme. In the NMMB, the boundary layer, and the free atmosphere turbulence are parameterized using the the Mellor-Yamada-Janjic (MYJ) turbulence closure scheme (Mellor and Yamada, 1982; Janjic, 2001). In the surface layer the Monin-Obukhov similarity theory (Monin and Obukhov, 1954) is applied (Janjic, 1996) in combination with a viscous sublayer parameterization over the oceans proposed in Janjic (1994). The wind speed at 10 m (U_{10}), which is the key parameter of almost all the implemented sea-salt production schemes is computed consistently with the surface layer parameterization. As usual, the friction velocity u^* is computed as the square root of the surface layer vertical momentum transport.

Grid-scale clouds are parameterized with the scheme of Ferrier et al. (2002), including 5 prognostic cloud variables. The relevant quantities for the coupling with aerosol processes are the mixing ratios of both liquid and ice cloud water and their conversion rates to precipitation. The Betts–Miller–Janjic convective adjustment scheme (Betts, 1986; Betts and Miller, 1986; Janjic, 1994, 2000) provides the coupling with sub-grid scale clouds. In this scheme, using conservational constraints, the convective clouds are represented by reference humidity and temperature profiles. Both water vapor mixing ratio and temperature are relaxed toward reference values within a convection timestep. In case of deep convection the reference profiles and the relaxation time are governed by the cloud efficiency E that depends on convective regime. This is a nondimensional parameter obtained as a combination of entropy change, precipitation, and mean cloud temperature (Janjic, 1994, 2000). The shallow convection parameterization closure uses the constraint that the entropy change must be nonnegative (Janjic, 1994, 2000). The Geophysical Fluid Dynamics Laboratory radiation package (Lacis and Hansen, 1974; Fels and Schwarzkopf, 1975) (GFDL) is implemented in NMMB in order to simulate the radiative transfer. Since the coupling with aerosols is not allowed by the operational GFDL scheme, the Rapid Radiative Transfer Model (RRTM) (Mlawer et al., 1997) was implemented in the model (Pérez et al., 2011). By using RRTM, it

is possible to couple radiation (both long- and short-wave) and aerosols by providing aerosol optical depth, asymmetry factor, and single-scattering albedo.

2.2 The BSC-CTM dust module (BSC-DUST)

The development of the sea-salt module follows the implementation of BSC-DUST (Pérez et al., 2011; Haustein et al., 2012) i.e. the dust module of NMMB/BSC-CTM. BSC-DUST was implemented as sectional approach with 8 transport bins ranging from 0.1 µm to 10 µm in dry radius. Within each transport bin a lognormal time-invariant sub-bin distribution is assumed. The processes considered by the module are dust emission, horizontal and vertical advection, horizontal diffusion and vertical transport by turbulence and convection, dry deposition and sedimentation, and wet removal including in- and below- cloud scavenging from grid- and sub-grid scale clouds. Water uptake was not considered. Given the strong uncertainties on the activation properties of dust, solubility is obtained by applying an intermediate hypothesis between pure hydrophobic and pure hydrophilic aerosol. Both global and regional simulations of dust optical depth have been exhaustively evaluated in Pérez et al. (2011) and Haustein et al. (2012). In this contribution, the model coarse AOD is calculated from the dust and sea-salt components allowing the use of AERONET stations affected by dust to be included in the evaluation. The dust simulations used are described in Pérez et al. (2011).

3 The sea-salt module

Sea-salt is assumed to be externally mixed with dust and the continuity equation is solved for 8 prognostic size-sections:

$$\partial_t q_k + (\mathbf{v} \cdot \nabla)_h q_k = F_k^{(emi)} - \sum_n F_{n,k}^{(sink)} + F_k^{(diff)} \tag{1}$$

where q_k are the average sea-salt dry mass mixing-ratios, $\mathbf{v}$ is the wind velocity, sub-script h stands for horizontal operator, and $F_k^{(emi)}$, $F_{n,k}^{(sink)}$, $F_k^{(diff)}$ represent sea-salt production, sink/mixing, and turbulent diffusion terms, respectively. Advection and diffusion are analogous to those of moisture in NMMB (Janjic, 2009). The production term is detailed in Sect. 3.1 and sink processes are described in Sect. 3.2.

Since the study of sea-salt cloud condensation nuclei is beyond the scope of the present work, we do not consider ultrafine particles and we assume a dry radius lower cutoff of 0.1 µm in the size distribution. We found in literature different upper size cutoff values, depending on the production parameterization (a detailed discussion is provided in Sect. 3.1). We fixed this value to 15 µm to comprehensively account for all the different formation processes. Size-bins are described in Table 1. Simulated sea-salt mass and optical depth are strongly influenced by the number of size-bins adopted, due to the strong dependence of dry deposition upon particle size (Witek et al., 2011). Simulated values tend to converge above 15 size-bins, while underestimates appear below that amount of bins. We chose to employ 8 size-bins which involves a mass loss of 5 % Witek et al. (2011) – a negligible quantity compared to emission uncertainties – as a trade-off for doubled computational efficiency. A sub-bin lognormal approach has been assumed in order to calculate different momenta of particle radius, such as the dry effective radius $r_d^{eff} = <r_d^3>/<r_d^2>$ and the volume mean radius $r_d^{vm} = (<r_d^3>/<r_d^0>)^{1/3}$. We assumed the canonical lognormal distribution of Lewis and Schwartz (2004), characterized by a geometric radius at RH = 80 % $r_{80}^g = 0.3$ µm and geometric standard deviation $\sigma^g = 2.8$.

3.1 Emissions

Strong uncertainties of up to one order of magnitude affect estimates of sea-salt production fluxes. The most used technique to parameterize the sea-salt emission flux is the so-called whitecap method. In this method, the flux is factorized as product of sea-surface whitecap fraction and production per whitecap unit, both terms affected

Modeling of the global distribution of sea-salt aerosol

M. Spada et al.

by significant uncertainities. Parameterizations found in literature use wind-speed at 10 m (U_{10}), sea-surface temperature (SST), atmospheric stability, sea-surface salinity, and ocean waves properties (height, age, relative direction respect to wind), for which Lewis and Schwartz (2004) and O'Dowd and de Leeuw (2007) provide useful reviews. For this study, we implement four of the most used whitecap method schemes for the open-ocean production (the surf-zone production is neglected here). Considered schemes are detailed in Table 2, where the labels G03, M86, SM93, and MA03 stand for Gong (2003), Monahan et al. (1986), Smith et al. (1993), and Mårtensson et al. (2003), respectively. G03, M86, and SM93 parameterizations are derived from observational datasets and only depend on U_{10} and MA03 from laboratory experiments also depending on SST. With the exception of the SM93 scheme, all the implemented schemes apply the same wind speed power law ($U_{10}^{3.41}$) in the whitecap parameterization. Consequently, in our work, we do not focus on the model sensitivity to changes in this term. The MA03 scheme was derived for a temperature interval ranging from 271 K to 298 K, which does not strictly cover the annual variation of global SST.

For our comparison, we choose schemes differing in particle-size and production mechanism description. Figure 1 shows that the strongest uncertainities appear for the ultrafine particles ($r_{d} < 0.1\mu$), which do not play a relevant role in the simulation of mass concentrations and optical properties and thus are beyond the scope of this work. The assumed lower cutoff value for the dry radius is 0.1 µm.

All considered schemes account for sea-salt formation from bubble bursting. Spume production is not described in M86 and MA03, while it is represented in SM93 (Fan and Toon, 2011), and its treatment in G03 is unclear. This leads to significant differences in emission fluxes of large particles (Fig. 1).

In addition, the above parameterizations were merged to obtain more comprehensive schemes, such as the combined M86/SM3 and M86/SM93/MA03 (Table 2). Hoppel et al. (2002) concluded that M86/SM93 may be considered as the best candidate to describe sea-salt emissions in the interval 0.15 µm to 15 µm in dry radius. M86/SM93

was then extended to ultrafine particles in other studies (Caffrey et al., 2006; Fan and Toon, 2011).

In this work, we also combine M86/SM93 and MA03 schemes to account for the dependence on the SST in the sea-salt production. In the implemented M86/SM93/MA93 scheme, the MA03 emission flux is applied in its range of validity and replaced by the M86/SM93 outside that range (i.e. for large particles with $r_d > 1.4\,\mu m$). We find a similar attempt in the work of Tsyro et al. (2011), where MA03 is combined with M86 (but not with the spume production of SM93).

We choose an upper cutoff for the particle size around the maximum value allowed by the sea-salt production parameterizations implemented in our module. To perform a consistent comparison, we considered a range of $[0.1–15]\,\mu m$ in dry radius for all the emission schemes, which implies an extension of M86 and G03 schemes beyond their formulation intervals. Because some schemes work with wet radius r_{80} and others with dry radius r_d, we assume $r_{80} = 2r_d$ to obtain emission of dry particles following the water-uptake treatment (detailed in Sect. 3.2). Mass emission fluxes $F^{(emi)}$ are calculated from number fluxes $F^{(emi)_N}$ as:

$$F_k^{(emi)} = \int_{bin-k} \frac{dF_N^{(emi)}}{dr_d} \cdot \frac{4\pi}{3} \rho_d r_d^3 dr_d \qquad (2)$$

The emission mechanism has not been explicitly coupled with the viscous sublayer of NMMB. However, the calculation of friction velocity and wind speed at 10 m depend on the viscous sublayer scheme in the surface layer.

3.2 Water-uptake

Sea-salt life cycle is strongly affected by water-uptake. Hygroscopic growth may increase particles radius by a factor of 4 or more. Following Chin et al. (2002) we introduce prescribed RH-dependent growth factors $\phi(RH) = r_w/r_d$, derived from the Global

Aerosol Data Set of Köepke et al. (1997) and the database of d'Almeida (1991) (Table 3). r_w and r_d are respectively the wet and the dry particle radius. r_w and r_d are respectively the wet and the dry particle radius. We assume the same factors for any radius-moment representation, such effective and volume-mean radius.

Given $\phi(RH)$, the water-uptake process is fully described by extending any dry particle parameter to its respective wet value. In particular we obtain wet particle radius and density as:

$$r_d \rightarrow r_w = \phi \cdot r_d \tag{3}$$

$$\rho_d \rightarrow \rho_w = f_d \rho_d + (1 - f_d)\rho_{water} \tag{4}$$

where ρ_{water} is the density of water and f_d is the volume fraction of dry aerosol ($f_d = \phi^{-3}$). The dry sea-salt density is assumed $\rho_d = 2160\,kg\,m^{-3}$ for every size-bin. By using this simplified approach, all aerosol processes affected by hygroscopic growth can be easily reformulated by extending the parameterizations used in the dust module (dry aerosol) to the wet-particles case, i.e. by applying Eqs. (3) and (4). In the following we present a short review of the parameterizations used by the aerosol module of NMMB/BSC-CTM, pointing out the extension to wet particles of sink and mixing terms. A more detailed description of each scheme can be found in Pérez et al. (2011). When not otherwise specified we refer to r_d^{vm} as r_d for brevity.

3.3 Deposition and convective mixing

Sedimentation is governed by the gravitational settling velocity $v_{g,k},(\phi)$, calculated for each size-bin k following the Stokes-Cunningham approximation. $v_{g,k},(\phi)$ depends on the particle size and thus on the water-uptake process: that dependence is underlined by the introduction of the parameter ϕ.

The dry deposition velocity $v_{dep,k}(\phi)$, acting at the bottom layer, is parameterized following Zhang et al. (2001). In this case, the dependence on ϕ here is introduced by the surface resistance calculation, which accounts for particle size and density (Slinn, 1982).

Title Page

Abstract | Introduction

Conclusions | References

Tables | Figures

|◄ | ►|

◄ | ►

Back | Close

Full Screen / Esc

Printer-friendly Version

Interactive Discussion

Wet scavenging fluxes are parameterized both for grid-scale (stratiform) and sub-scale (convective) clouds. In-cloud and below-cloud scavenging from grid-scale clouds are calculated by coupling with cloud microphysics scheme of Ferrier et al. (2002) implemented in NMMB. In-cloud scavenging flux is parameterized within the use of a solubility parameter e_k, that is defined as the fraction of aerosol contained in cloud which may eventually precipitate. For sea-salt particles, e_k is obtained from Zakey et al. (2006). Since the values found in Zakey et al. (2006) for dust represent an intermediate between pure hidrophobic and pure hydrophilic hypothesis, we assume $e_{ss,k} = 2e_{du,k}$. This calculation of $e_{ss,k}$ is well supported by the values used by other state-of-the-art models (see for ex. the sensitivity study in Fan and Toon, 2011). Because small particles are more probable candidates to act as cloud condensation nuclei, $e_{ss,k}$ decrease with size (see Table 4). Grid-scale below cloud scavenging is parameterized following Slinn (1984): such parameterization implies the calculation of capture efficiencies $E_k(\phi)$, which in their turn depend on the wet radius and density of the aerosol particles.

For sub-grid (convective) clouds, the scavenging fluxes are coupled with the Betts–Miller–Janjic scheme (BMJ) of NMMB. The convective in-cloud scavenging parameterization employs as well solubility factors $e(k, \phi)$. After the in-cloud scavenging, the remaining sea-salt is assumed vertically mixed by performing a conservative relaxation towards reference profiles. The parameterization of sub-grid below-cloud scavenging is analogous to the case of grid-scale clouds. Within shallow non-precipitating convective clouds sea-salt is homogeneously mixed within the cloud.

3.4 AOD calculation

In order to calculate the sea-salt optical depth, extinction efficiencies $Q^{\text{ext}}_{\lambda,k}$ were computed by using the Mie-theory solving algorithm of Mishchenko et al. (2002) for each size-bin k and at each RH-value related to the growth factors, i.e. as a function of ϕ (extinction efficiencies at $\lambda = 500\,\text{nm}$ are shown in Fig. 2). Spherical homogeneous particles are assumed. Extinction efficiencies also depend on the sub-bin lognormal geometric parameters r^g and σ^g (Lewis and Schwartz, 2004). The optical depth is

Title Page

Abstract | Introduction

Conclusions | References

Tables | Figures

|◄ | ►|

◄ | ►

Back | Close

Full Screen / Esc

Printer-friendly Version

Interactive Discussion

obtained as:

$$\tau_{\lambda,k} = \beta_{\lambda,k}\tilde{M}_{d,k} \tag{5}$$

where $\tilde{M}_{d,k}$ is the layer dry mass loading of each bin and $\beta_{\lambda,k}$ is a mass extinction coefficient which accounts for water-uptake:

$$\beta_{\lambda,k} = \frac{3Q_{\lambda,k}^{ext}(\phi, r_w^g, \sigma_w^g)}{4r_{w,k}^{eff} f_d(\phi)\rho_{d,k}} \tag{6}$$

The algorithm of Mishchenko et al. (2002) also provides single-scattering albedo and asymmetry factor for radiative calculations. The total sea-salt optical depth is obtained by taking the sum over all the bins:

$$\tau_{\lambda,T} = \sum_{k=1,8} \tau_{\lambda,k} \tag{7}$$

Additionally, in order to perform a comprehensive comparison with observations, we calculate a coarse sea-salt optical depth by assuming a lower cutoff value of $0.6\,\mu m$ (the AERONET submicron cutoff) for the wet particle radius. In our description, this values is equivalent to a lower cutoff for the dry particle radius $\bar{r}_d$ given by:

$$\bar{r}_d = 0.6\,\mu m/\phi(\text{RH}) \tag{8}$$

Sub-bin contributions to the coarse optical depth are calculated by applying the log-normal distribution of Lewis and Schwartz (2004). Another useful parameter for model evaluation is the resulting AOD (total and coarse) from both sea-salt and dust. Because of their external mixing, we assume:

$$\tau_{ss+du,\lambda} = \tau_{ss,\lambda} + \tau_{du,\lambda} \tag{9}$$

where the subscripts ss and du respectively refer to sea-salt and dust.

4 Observational data

Figure 3 displays the location of measurement sites and cruise measurement pathways used in the evaluation of the model. Names and coordinates of the sites are listed in Table 5. Quantities evaluated are sea-salt surface concentrations and AOD. For the station data we use monthly climatologies and monthly averages of 2006, our reference year. The simulated annual mean wind speed at 10 m is also compared with QuickSCAT satellite observations.

We consider AERONET Sun photometer measurements as the reference to evaluate the modeled sea-salt AOD. Even if algorithms tend to minimize biases due to cloud cover and other effects (e.g. Zhang and Reid, 2006), estimates from satellites remain highly uncertain and are not used in this contribution. Satellite overestimates can reach up to 0.07 in island stations compared to monthly AERONET-derived AOD (Jaeglé et al., 2011). At certain latitudes, the bias between satellite and ship AOD measurements may range from −0.2 to +0.2 (Smirnov et al., 2011). These biases exceed the typical value of the sea-salt AOD in the remote marine environment ($\sim$ 0.07, see Smirnov et al., 2011).

4.1 QuikSCAT-SeaWinds: 10 m-windspeed

Sea-salt emissions are strongly influenced by surface wind speeds. We compare the model annual mean U_{10} for the reference year (2006) against observations from the NASA SeaWinds scatterometer aboard the QuikSCAT satellite (Dunbar et al., 2006). Level 2B science-quality data provided by QuickSCAT at 1 degree of horizontal resolution is bilinearly interpolated to the model grid.

4.2 NOAA/PMEL cruises surface concentrations

Sea-salt cruise measurements are considered, specifically ions concentrations from two cruises of the NOAA Pacific Marine Environmental Laboratory (PMEL): the

AEROSOLS99 and INDian Ocean EXperiment (AEROINDOEX) in 1999 spanning the Atlantic and the Indian Oceans and the first Aerosol Characterization Experiment (ACE1) in 1995 crossing the Pacific Ocean. Concentrations of both Na^+ and Cl^- were measured by ion chromatography (Quinn et al., 1998) at 18 m above the sea surface. The experimental aerodynamic cutoff diameter was 10 μm for all the cruises. Instruments were kept at constant RH values during measurements. Based on these values, Jaeglé et al. (2011) assumed a dry radius cutoff of 3 μm for AEROINDOEX and ACE1. Hence, we use the first 6 dry model bins for the comparison. The ACE1 and AEROINDOEX datasets also provide wind speed measurements, at 33 m and 14 m above sea surface respectively.

The spatial scale of the cruise measurements is around 600 km since they were averaged over temporal windows ranging from 2 to 24 h and mean ship speeds were around 24 km h^{-1}.

4.3 U-MIAMI surface concentrations

The University of Miami (U-MIAMI) network has supplied aerosol measurements at around 35 stations over the world from the early 1980s until 1996 (Savoie and Prospero, 1977). Aerosols were collected by high-volume filter samplers and different measurement protocols were employed depending on the measurement site. For our comparison, we use climatologies obtained from this dataset in 15 stations (see Fig. 3 and Table 5). These stations grant good data quality and are not affected by surf-zone production (J. Prospero, personal communication, 2012). The observed sea-salt mass concentrations ($\mu g\,m^{-3}$) are computed as $SS = Cl^- + 1.47Na^+$ following Quinn and Bates (2005) where both Cl^- and Na^+ measurements are available, and as $SS = 3.252Na^+$ where only Na^+ concentrations are supplied (J. Prospero, personal communication, 2012). Since the U-MIAMI measurements are not constrained by an upper cutoff in radius, we perform the comparison by using the complete set of model bins.

4.4 AERONET AOD

The AEROsol RObotics NETwork (AERONET) provides automatic ground-based observations from Sun photometers in a large number of stations around the globe (Holben et al., 1998; Smirnov et al., 2000). We consider a set of 17 sea-salt dominated stations as proposed by Jaeglé et al. (2011) (Fig. 3 and Table 5). The three requirements fulfilled by the stations are sea-salt contributions greater than 50 % to the total AOD as predicted by GEOS-CHEM model, availability of Level 2 quality-assured data for all the considered time ranges, and at least 3 yr of data supporting the monthly climatologies. We chose 2006 as the reference year because it was characterized by the largest number of active stations among the 17 selected. The evaluation is performed against monthly climatologies and monthly means for 2006 of the AOD at 500 nm. In particular, we focus on the AOD coarse fraction, therefore avoiding the influence of fine aerosol species. To ensure consistency in the comparison, we calculate the model coarse AOD by assuming the same cutoff value as the AERONET Spectral Deconvolution Algorithm (SDA), i.e. 0.6 μm in wet effective radius (O'Neill et al., 2008).

5 Results

5.1 Global simulations

5.1.1 Experimental setup

We performed global simulations at two horizontal resolutions: $1° \times 1.4°$ and $0.333° \times 0.469°$ identified by the labels GLOB(L) and GLOB(H), respectively. 24 vertical layers were employed and the dynamics timestep is set to $\Delta t = 120$ s for GLOB(L) and $\Delta t = 60$ s for GLOB(H). Meteorological conditions were initialized every 24 h using the NCEP final analyses (FNL) at $1° \times 1°$ from ≥ 2000 and the NCEP Global Data Assimilation System analysis (GDAS) at $2.5° \times 2.5°$ before the 2000. A spinup of 1 month for

sea-salt was assumed at the beginning of the simulated period. In the simulation of the reference year (2006), the model output was taken every 6 h to calculate monthly means, while the model values are computed every 1 h when comparing against cruise observations.

5 The four implemented emission schemes are compared against comprehensive datasets of observations dispersed over the globe. As reported in Table 1, we refer to them respectively with the labels: G03 for Gong (2003), M86 for Monahan et al. (1986), M86/SM93 for the combined M86 with Smith et al. (1993), and M86/SM93/MA03 for the combined M86/SM93 with the SST dependent scheme of Mårtensson et al. (2003).

10 The dust contribution to the AOD is indicated with the label DU. An accurate assessment of the ability of NMMB/BSC-CTM in simulating the dust life cycle at global scale can be found in Pérez et al. (2011).

Feedback processes between aerosols and radiation were not considered in all the simulations conducted in this work.

15 **5.1.2 Global wind speed**

The model was compared against measurements from the QuickScat satellite for the reference year 2006. The bias between model and satellite U_{10} is shown in Fig. 4 for GLOB(L). Although far from being an exhaustive evaluation of the NMMB's ability to reproduce the wind speed at 10 m, the comparison provides an general estimate of the 20 model performance. The mean annual bias ranges between $-0.5\,\mathrm{m\,s^{-1}}$ and $+0.5\,\mathrm{m\,s^{-1}}$ over most of the globe. Only in small regions close to coastal areas, overestimates reach up to $+1\,\mathrm{m\,s^{-1}}$. Relevant underestimates of $-1\,\mathrm{m\,s^{-1}}$ or more are found in the equatorial convergence zone, although satellite measurements may be affected by positive biases compared to buoy observations in this region (Quilfen and Chapron, 25 2001; Bentamy et al., 1997). Overall, we find a mean normalized bias of -5.4% over the whole domain and a mean normalized gross error of 6.3%. An increase in model horizontal resolution (GLOB(H)) leads to similar global patterns, with a slight reduction of bias (-4.3%) and gross error (5.2%).

5.1.3 Global sea-salt distribution and total budgets

We analyze the global distribution of simulated mean sea-salt emissions, surface concentrations and AOD at 500 nm. As displayed in Fig. 5, there is a pronounced asymmetry in the summer-to-winter variation between the two hemispheres. Sea-salt global patterns are characterized by four regions of maximum production. The two most important peaks of monthly mean values are found in regions with enhanced westerlies, i.e. beyond the horse latitudes (lat > 30° N and lat < 30° S). Also two local maxima can be observed in correspondence to the trade winds, next to the intertropical convergence zone (around 10° N and 10° S). While sea-salt production at the southern belt only slightly changes with season, the northern belt is affected by strong variations during the year with an increase of +150 % in emission flux, surface concentration, and AOD. It is well known that these two seasonal regimes are related to the asymmetric variation of the global wind speed pattern, which is due to the variation in the global atmospheric angular momentum (Sandwell and Agreen, 1984). In our case, sea-salt is additionally boosted through the wind power-laws in sea-salt emission schemes.

An additional remark concerns the simulated maximum values along the trade winds. During winter over the Pacific region in Fig. 5, sea-salt production and surface concentration around 10° N is about half the values found at higher latitudes. However, the AOD reaches monthly mean values close to the global maximum. Trade winds are characterized by dry conditions with a low wet scavenging rate increasing particle lifetime, in contrast to the strong production belts characterized by wet extratropical cyclone activity. The RH-dependent particle size and optical properties in the model also play a relevant role in determining the AOD peaks close to the intertropical convergence zone.

Figure 6 displays maps of annual mean sea-salt emissions, surface concentration, and AOD with the four implemented emission schemes. In terms of absolute values, the two maximum production regions beyond the horse latitudes are the most sensitive to the choice of emission scheme. The G03 scheme produces the highest concentrations

(with peaks above 40µg m^{-3} in the southern belt and over 25µg m^{-3} in the northern belt). Differences in the spume production representation can be appreciated by comparing the patterns obtained with the simple M86 against M86/SM93, for which the mean concentration is enhanced due to wind episodes exceeding the threshold $U_{10} > 9\,\text{m s}^{-1}$. The SST dependence in M86/SM93/MA03 produces a latitudinal modulation of the emission fluxes and surface concentration with relative enhancement in the tropics and reduction elsewhere.

Sea-salt AOD patterns with M86, M86/SM93, and G03 schemes are very similar. The southern belt dominates with peaks around ~ 0.1–0.125. Peak values around ~ 0.075 are found at high latitudes and the tropical Pacific. Relevant differences are observed with the M86/SM93/MA03 scheme for which absolute maximum values around 0.125 appear next to the intertropical convergence zone. These peaks overestimate maximum AOD from ship measurements gathered by Smirnov et al. (2011) both in the remote tropical Pacific (0.07 for total AOD at 500 nm) and the Indian Ocean (0.06, east of Madagascar).

Table 6 lists the model budgets with the different emission configurations. In particular, we note that the particle lifetime and the fraction of wet to total deposition are sensitive to the size distribution of the emission flux. The lifetime ranges from 7.7 hours with the G03 scheme, in which large spume particles are emitted independently from wind conditions, to 12.0 hours with the simple M86 scheme, in which spume production is neglected. Due to an overall increase in production of fine particles, the M86/SM93/MA03 related values slightly exceed those for the M86/SM93 scheme.

Regardless of the choice of emission scheme, the total budgets for year 2006 are in agreement with those obtained by the AEROCOM median model for year 2000 (Textor et al., 2006).

Modeling of the global distribution of sea-salt aerosol

M. Spada et al.

Title Page

Abstract	Introduction
Conclusions	References
Tables	Figures

|◄ | ►|
◄ | ►

| Back | Close |

Full Screen / Esc

Printer-friendly Version

Interactive Discussion

5.1.4 Modeled surface concentrations against cruise data

The cruise measurements provided by the NOAA/PMEL vessels allows a comparison between model and observations at timescales of [2–24] hours. Each measurement gathered by the vessels was averaged on space and time, thus we note that simulated values may be affected by spurious errors due to the adopted spatio-temporal averaging technique. We remapped the original lat/lon grid at (L) resolution (Δx, $\Delta y = 1°$, $1.4°$) to a coarser resolution ($\Delta x' = n\Delta x$, $\Delta y' = n\Delta y$), matching the characteristic spatial length of the cruise under consideration. For this comparison, we do not use the GLOB(H) resolution. The number n is defined as the smallest integer satisfying the following conditions:

$$V_{\text{cruise}} \cdot \max(T_{\text{obs}}) < n\Delta x \tag{10}$$
$$V_{\text{cruise}} \cdot \max(T_{\text{obs}}) < n\Delta y \tag{11}$$

where V_{cruise} is the vessel mean speed during the cruise and T_{obs} is the observation duration, which is not constant. In this way, the spatial extent of each measurement is represented by a single lower resolution gridcell. We use $n = 2$ for AEROINDOEX and $n = 4$ for ACE1. Model outputs every 1 h were then averaged over each measurement period. Cruise trajectories are displayed in Fig. 3. We recall that the values shown in this comparison refer to an upper cutoff of 3 μm in dry radius, thus we investigate the model's ability to simulate the concentration within the first 6 bins. In this sense the M86/SM93 scheme is equivalent to the M86 scheme, since the larger particles produced by spume cutting are not taken into account due to the observational cutoff.

Figure 7 shows a good overall correlation for AEROINDOEX and a lower correlation for ACE1. Our results are similar to those obtained by Jaeglé et al. (2011) and Witek et al. (2007) by using the GEOS-CHEM and the NAAPS models, respectively. The AEROINDOEX campaign is simulated with a correlation of 0.60 with both M86 and G03 schemes. The correlation decreases when employing the SST-dependent M86/SM93/MA03 scheme (0.49). The mean normalized bias ranges from +0.4 %

(M86/SM93/MA03) to −36.8 % (G03) showing an overall tendency of the model to-wards underestimation, which is mainly due to errors in reproducing the peak around day 25. The mean normalized gross error is around 60 % for all cases.

For ACE1, the model's correlation is low (around 0.36) regardless of the emission scheme applied. There is an overall positive bias between model and observations ranging from +15 % (G03) to 34.7 % (M86/SM93/MA03). The gross error is around 50 % or more. Because of the larger measurement timescales of ACE1, larger errors in the simulated values may be partly due to the inefficiency of the averaging tech-nique. In Fig. 7 we show also the comparison between the simulated wind speed at 10 m and the cruise measurements (which are performed at around 18 m above the sea surface). The measurements are 30 min-averages while the model output is taken every 1 h as an instantaneous value for both cruises (model SST values intercepted by the cruise trajectories are overlapped on the wind speed panels). An additional issue concerns the performance of the model wet deposition parameterization. We identify that the model errors in the simulation of the concentration peak around day 25 of the AEROINDOEX cruise are to a large extent due to overestimates of the wet deposition flux.

Summarizing, the SST-dependent emission scheme (M86/SM93/MA03) does not im-prove the simulation of the considered cruise campaigns compared to the M86 and G03 schemes and leads to a worse correlation. On the other hand, the model performances achieved by M86 and G03 schemes are very similar.

5.1.5 Model surface concentrations against U-MIAMI measurements

Modeled monthly mean surface concentrations for year 2006 are compared against climatologies from 15 stations of the U-MIAMI network (see Fig. 8). Model values are in an overall good agreement with the observed climatologies in Bermuda (b), Cape Grim (c), Cape Point (d), Miami (l), Midway Island (m), Oahu (n), and Reunion Island (p). Significant model overestimates are found in Baring Head (a), Chatam Island (e), Invercargill (g), King George Island (h), Marion Island (i) and Palmer (o).

Since Baring Head (a), Chatam Island (e), Invercargill (g), and Marion Island (i) are located in regions characterized by complex topography, we hypothesized that surface concentration overestimates in these stations may at least in part due to the low global model resolutions used. This hypothesis is investigated in detail in Sect. 5.2 for Baring Head (a), Chatam Island (e), and Invercargill (g) located in New Zeland and complemented by high resolution simulations in Marion Island (i) which are shown in the Supplement. Overestimates in King George Island (h) and Palmer (o) could be at least in part due to an incorrect model representation of the Antarctic sea/ice interface at the simulated resolutions.

Significant model underestimates are found in Fanning Island (f) and American Samoa (q) which are located in the tropical Pacific. In this region, errors in the description of the large particles production cannot be excluded. As shown in Fig. 8, there is a significant influence of the applied emission scheme upon the modeled sea-salt surface concentrations. To summarize this comparison, we provide scatterplots of observed vs simulated values in Fig. 9. We neglect in these plots the contributions from Baring Head (a), Chatam Island (e), Invercargill (g), King George Island (h), Marion Island (i), and Palmer (o). This reduces the set of available stations from 15 to 9 but in this way we keep the comparison at least in part free from errors due to the model representation of topography/ice-cover at global scale. Additionally, the plots are accompanied by a linear regression fit for each scheme. The fit is weighted according to the interannual standard deviations. We underline that these results should be taken with caution due to the climatological nature of the observed means. Fig. 9 indicates that the G03 scheme generally overestimates the climatological monthly mean concentrations, while the M86 underestimates. The best agreement is obtained with the M86/SM93 and the M86/SM93/MA03 emission schemes. Overestimates with the G03 scheme may be explained by its unclear description of spume particles production, as already noted in Fan and Toon (2011). Indeed, the emission flux with the G03 scheme for particles larger than $10 \mu m$ in dry radius is nearly one order of magnitude larger than in the other implemented schemes (Fig. 1). On the other hand, the spume production is

not considered in the M86 scheme, and this may partly explain the underestimated concentrations. The introduction of spume particles in the combined M86/SM93 improves the model results (Fig. 9). This improvement is more evident in stations and months characterized by frequent episodes of wind speed greater than $9\,\mathrm{m\,s^{-1}}$, such as for example during January, February and March in Bermuda (b) (Fig. 8). In the tropics, where these episodes are infrequent, M86 and M86/SM93 provide similar results. The introduction of the SST-dependence in the emission scheme M86/SM93/MA03 does not provide improvements compared to M86/SM93 (Fig. 9).

5.1.6 Aerosol optical depth

Simulated coarse AOD monthly means for year 2006 are compared against monthly climatologies at 16 AERONET sites (Fig. 10). The coarse AOD simulated by the model is overall in agreement with the observed climatologies. Significant discrepancies are found in Ceilap-RG (6), Crozet Island (8), Dunedin (9), and Reunion Island (14). Overestimation in Ceilap-RG (6) affects the entire yearly cycle due mostly to errors in dust aerosol emissions in South America. When neglecting the dust contribution in this location, the nearly constant yearly cycle and its mean value (~ 0.02) are well reproduced. Overestimation in Crozet Island (8), Dunedin (9), and Reunion Island (14) stations take place mainly during austral winter (JJA). At Crozet Island (8) and Dunedin (9) the model peaks are partly related to enhanced westerlies during these months. At Reunion Island (14) and Dunedin (9) the significant dust influence in the model leads to uncertainities in the comparison. At Ascension Island (2), Bermuda (4), Cape San Juan (5), La Parguera (11), and Midway Island (12), the model's ability to reproduce the dust cycle is decisive for a proper simulation of the coarse AOD.

Simulated coarse AOD are compared against a subset of 5 sites with observations avalaible in 2006 (Fig. 11). Ceilap-RG (6) is excluded from Fig. 11 because of the overestimates due to dust. With the exception of Nauru (13), results are similar to those obtained using climatologies (Fig. 10), since the reference year is close to the climatological behavior. Table 7 displays model statistical scores for each production

scheme and for each available station in 2006. Overall emission schemes show correlation coefficients around ~ 0.8, a positive mean normalized bias of about $\sim 20\%$ and an overall mean normalized gross error of $\sim 40\%$. Results outline a close behavior among G03, M86 and M86/SM93 schemes, in contrast to the SST-dependent scheme M86/SM93/MA03, which overestimates AOD over warm sea-surfaces in the tropics (e.g. Guam Island (10) among others) and to a lesser extent at high latitudes (e.g. Crozet Island (8) and Ceilap-RG (6)). These results are related to differences in emitted size-distributed fluxes and the hygroscopic growth of sub-micron aerosols affecting the coarse AOD. Figure 1, shows close to an order of magnitude difference in the number emission flux for particles with dry radius in the range $0.15\,\mu m - 1.4\,\mu m$. Hygroscopic growth of particles above $0.6\,\mu m$ adds up to explain the higher coarse AOD when using the SST-dependent scheme. As implemented in this work, SST dependence in the sea-salt emission parameterization is not leading to a better agreement of the model AOD with observations.

In order to facilitate the discussion, we produce the scatterplot in Fig. 12 (where the Ceilap-RG (6) station is excluded, due to the errors in the dust AOD). As shown in Fig. 12, we find that the use of the M86/SM93/MA03 scheme produces an overall overestimation of the climatological monthly mean coarse AOD values provided by AERONET, while a better agreement is obtained when using the other emission schemes. As already stated in the previous subsection, these results should be taken with caution due to the climatological nature of the observed means. As an example, we recall the opposite results obtained in Nauru (13) when the M86/SM93/MA03 is compared to climatologies (Fig. 10) and year 2006 (Fig. 11). In any case, the measurements provided by the subset of active stations in the 2006 seem to confirm our previous remarks. As shown in Table 7, G03, M86 and the combined M86/SM93 emission schemes provide quite similar overall performances (normalized bias around +20%, mean normalized gross error around 40%, and temporal correlation around 0.8.), while the use of the M86/SM93/MA03 scheme produces an overall increase in bias and gross error (+66.0% and 71.5%) and a worse correlation (0.61). By using the SST-dependent

emission scheme we obtain significant errors in Guam Island (10) and Midway Island (12) (correlations of 0.02 and 0.36, respectively). In Nauru (13), the SST-dependent scheme leads to a marked increase of bias and gross error, but the correlation remains similar to that obtained with the other schemes (around 0.85). Undestanding when the use of SST-dependent sea-salt emissions may improve the simulated AOD or just compensate for other model errors is complex. Guam Island (10), Midway Island (12) and Nauru (13) are located in the tropics and they are characterized by similar sea surface temperatures. However, we obtain different performances using the M86/SM93/MA03 scheme in these stations.

5.1.7 Discussion

We provide an integrated summary of the evaluation of simulated surface concentrations (Figs. 7, 8 and 9) and coarse AOD (Figs. 10, 11, and 12). The introduction of an additional parameter (SST) in the production scheme worsens the estimation of coarse AOD from AERONET (Table 7) and surface concentrations during AEROIN-DOEX (Fig. 7). We underline that since the SST-dependent scheme used in our work (M86/SM93/MA03) is a combination of the MA03 scheme with other schemes covering the entire particle size interval, inconsistencies due to the merging may be at play. We also note that we evaluate the model performance with different sea-salt emission schemes without "a-posteriori" improvement techniques, such as the SST-based adjustment proposed by Jaeglé et al. (2011).

The other three implemented schemes (G03, M86, M86/SM93) provide similar simulated AOD values (Figs. 10, 11, 12, and Table 7) but show significant differences in simulated surface concentrations (Figs. 7, 8, and 9). With regard to the comparison of the entire size-bin interval surface concentration with U-MIAMI climatologies, significantly better results are obtained with M86/SM93 scheme compared to M86 and G03, which is in agreement with the conclusions of Hoppel et al. (2002). This could be due to the treatment of spume particles in the production flux, which is not taken into account

in M86 and is unclearly represented in G03. Note also that both M86 and G03 schemes were extended beyond their range of validity.

5.2 Regional high resolution simulation in New Zeland

When comparing the performances obtained by increasing the global horizontal resolution from $1° × 1.4°$ (GLOB(L)) to $0.333° × 0.469°$ (GLOB(H)) we found an overall low sensitivity particularly for the AOD (see Fig. 10 and Fig. 11). The exception is Ceilap (6), but due to the errors in the dust simulation in this region we exclude it from the discussion. For surface concentration (Fig. 8), we obtain quite similar results in most of the stations, but significant differences (up to -50%) are found in Inverncargill (g) and Palmer (o), where the simulated values are slightly improved by the increase in resolution which suggests that small scale phenomena in these regions may not be well captured by the model at low global resolutions.

In order to investigate small-scale effects in sea-salt estimates, we performed a regional high resolution simulation in a domain covering the region of New Zeland where 3 U-MIAMI stations are located, namely Baring Head (a), Chatam Island (e), and Inverncargill (g). We hypothesized that the strong discrepancies between model and observations (see Fig. 8) could be due to the model inability to capture the characteristic scales introduced by the complex topography of this region.

In this section, we evaluate the simulated sea-salt aerosol and we analyze the wind speed at 10 m and precipitation compared to the global low resolution simulation. This section is more intended as a test case discussion rather than an exhaustive evaluation of the model performance at regional scale.

The interaction between the New Zealand Southern Alps and atmospheric dynamics and physics represents a classic example of the barrier problem (see Roe, 2005, for an exhaustive review of this issue). In this region, open ocean westerlies and extratropical cyclones collide with the steep orographic gradients of the Southern Alps. The influence of New Zealand's orography upon wind and precipitation patterns is well studied both experimentally (Sinclair et al., 1997; McCauley and Sturman, 1999; Wratt et al., 2000)

and through regional modeling (Katzfey, 1995a,b; Bormann and Marks, 1999; Revell et al., 2002).

The Southern Alps are around 40 km wide and over 1.5 km high (maximum height of 3 km). Hence, at GLOB(L) ($1° \times 1.4°$) and GLOB(H) ($0.333° \times 0.486°$) resolutions, we were trying to solve their gradients with an horizontal length lower ($\lambda_L/\lambda_c < 1$) or barely similar ($\lambda_H/\lambda_c \sim 1$) to the characteristic one ($\lambda_c = 40$ km; λ_L and λ_H are the horizontal spatial scales characterizing the two resolutions). This treatment may lead to significant errors in the simulations of both meteorological and aerosol variables. In order to properly solve this kind of gradients, we increased the horizontal resolution up to $0.1° \times 0.1°$. In this way, we obtain $\lambda_R/\lambda_c \sim 5$ (λ_R is the regional gridcell length). Consequently, we chose a timestep of $\Delta t = 20$ s. We simulated the 2006 year. Meteorological initial conditions were initialized every 24 h using the NCEP final analyses (FNL) at $1° \times 1°$; meteorological boundary conditions were updated every 6 h using FNL. We used 24 vertical layers.

Because aerosol boundary conditions for the regional domain were not implemented in the model at this stage of development, we set the domain boundaries far from the region in study, i.e. at least 400 km far from the nearest U-MIAMI station. With a rough calculation, we estimate that this distance is inferior than the average sea-salt average lifetime (see Table 6) multiplied by the maximum annual mean wind speed value reached in the domain (i.e. ~ 11 h·36 km h^{-1} = 396 km). In this way the errors introduced by the absence of sea-salt boundary conditions are not substantially affecting the inner part of the domain.

In the following, we use the label REG for this regional model setup. We use the M86/SM93 emission scheme in this simulation.

As shown in Fig. 13, we obtain very significant improvements with the REG simulation. In each station, the monthly mean surface concentrations decrease by a factor of 2 or more with respect to GLOB(L) and GLOB(H), matching the observed climatological values.

We detect two different effects that explain the results obtained. A first effect can be clearly distinguished at Chatam Island (e) where there is a nearly constant shift of the simulated concentrations towards the observations, with the annual trend more or less conserved. This is due mainly to the ability of the high resolution model to properly solve the sea-land interface, i.e., at GLOB(L) and GLOB(H) resolutions the island is represented by a sea gridcell where emission occurs, while at REG resolution the station lays over a land gridcell. This underlying effect affects model results whenever comparing against coastal stations.

A second effect can be observed in Baring Head (a) and Inverncargill (g). Here we find not only a decrease in concentration, but an evident modification of the annual trend. We relate this effect to the meteorology-orography interaction in the region. The uneven annual trends simulated at low resolution, with strong peaks in the austral spring (October), are smoothed when the REG scales are used as the gradients introduced by the Southern Alps range are properly resolved.

Figure 14 presents annual mean sea-salt surface concentration, annual mean wind speed, and annual accumulated precipitation over the area of interest for REG and GLOB(L) runs. We clearly observe that the relative surface concentration difference between REG and GLOB(L) is between −20% and −10% in the region surrounding Chatam Island. A 40% decrease is found only at the island gridcell. On the other hand, we observe that the Baring Head (a) and Inverncargill (g) stations both fall along the wide concentration decrease pattern surrounding New Zealand.

The difference of concentration patterns within the domain can be explained by the differences in wind speed and precipitation (Fig. 14). In particular we note that, even if the simulated wind speed over the sea surface (and thus sea-salt production) increases with resolution over some regions (i.e. over the Cook strait in the middle, over the Bay of Plenty in the north-east, and over the coast in front of the Tasman Sea in the southwest), concentrations are reduced overall. This is due to the dominant role played by precipitation and its relationship to the strong orographic gradients. As shown in Fig. 14, we observe a windward (western subdomain) enhancement of precipitation stronger

than leeward (eastern region). If we roughly assume wet removal as proportional to precipitation, we find an increase from 20 % to 40 % or more of this sink when increasing the resolution from GLOB(L) to REG, due to the effect of the orographic barrier. This asymmetry is reflected in the surface concentration difference patterns. Observed climatological precipitation in New Zeland (Wratt et al., 2000) confirm our high resolution precipitation estimates in the western coastal area (model: $\sim 3\,\mathrm{m\,yr^{-1}}$, measurements: 2–3 $\mathrm{m\,yr^{-1}}$), upwind of the barrier (model: $\sim 10.5\,\mathrm{m\,yr^{-1}}$, measurements: 11–12 $\mathrm{m\,yr^{-1}}$), and over the eastern lands (model: $< 1.5\,\mathrm{m\,yr^{-1}}$, measurements: $< 1\,\mathrm{m\,yr^{-1}}$). Complementing this discussion, in the Supplement we present results of a regional simulation centered over the Marion Island (i) station as another example where the orographic effects are well resolved by the model at higher resolution.

Summarizing, the simulated sea-salt concentration is very sensitive to the model representation of orographic gradients. While the sea-land interface effect is affecting only coastal areas, significant differences ranging from −10 % to −40 % over the sea-surface can take place even far away from the orographic barrier, affecting spatial scales typical of global simulations (up to 10° or more). Over land, both windward and leeward of the barrier, differences of −40 % or more are found.

The results presented in this section show that, even at a resolution of 0.333° × 0.469°, the model is still unable to properly capture the surface concentration in the New Zealand region.

6 Conclusions

We presented simulations of the sea-salt aerosol global distribution with the multiscale model NMMB/BSC-CTM. Since the main uncertainties in the sea-salt modeling are related to the parameterization of emissions, we implemented four different sea-salt emission schemes in order to analyze their performance. We compared a global reference simulation of year 2006 against climatologies from the U-MIAMI and "sea-salt dominated" stations from the AERONET sunphotometer network. For the comparison

against AERONET, we used the coarse fraction of the AOD. We also compared the simulated monthly mean AOD against measurements gathered during the 2006 from a subset of the considered AERONET stations.

The use of M86, M86/SM93, or G03 emission schemes leads to similar results in the simulation of the monthly mean coarse AOD (correlation around 0.8 in the reference year). On the contrary, the simulated surface concentrations may significantly differ depending on the applied scheme. In particular we find a slight but relevant model improvement when the M86/SM93 scheme is used that may be related to its specific description of spume particles.

The implementation of the SST dependence in the M86/SM93/MA03 scheme did not improve the model performance. In particular, we found significant overestimates in the simulation of the coarse AOD fraction and a decrease in correlation (0.6 in the reference year). The comparison against cruise measurements from two campaigns of the NOAA/PMEL group tended to confirm the above conclusions. The model sea-salt lifetime range from 7.7 h to 12.0 h, depending on the emission scheme. In any case, these values are close to those simulated by the AEROCOM median model for the year 2000.

Taking advantage of the multiscale core of the model, we performed a regional simulation at 0.1° within a domain centered around New Zealand including three U-MIAMI stations (Baring Head (a), Chatam Island (e), and Inverncargill (g)) that were strongly overestimated in the global simulation. Rather than providing a detailed evaluation at regional scale, our interest in this case was to investigate the influence of model resolution upon sea-salt aerosol processes in a region characterized by complex orography. We find both a concentration decrease of up to 40% and a smoothing of the annual trend that matched significantly better the climatological observations. The concentration decrease was mainly driven by a combined modification of wind speed and precipitation patterns produced by a better resolution of the barrier gradients. A better resolution of the sea-land interface also played a role when comparing against data from coastal stations. However, the difference between regional and global values extends

Modeling of the global distribution of sea-salt aerosol

M. Spada et al.

Title Page

Abstract | Introduction

Conclusions | References

Tables | Figures

◄ | ►

◄ | ►

Back | Close

Full Screen / Esc

Printer-friendly Version

Interactive Discussion

to most of the simulated domain (ranging from 10% to 40%). We relate this difference to the overall increase in precipitation (and consequently in aerosol wet deposition) in the regional simulation which matches well the precipitation climatology in the region. Our results outline that caution may be taken when evaluating and/or constraining mod-
5 eled sea-salt concentrations at global scale in regions affected by coastal/orographic effects.

The development of the sea-salt module of the NMMB/BSC-CTM is a a step further towards an aerosol model, including dust (Pérez et al., 2011), black and organic carbon, sulfate, and its online coupling with the gas-phase chemistry (Jorba et al., 2012)
10 to obtain a unified online multiscale chemical weather forecasting system.

Supplementary material related to this article is available online at: http://www.atmos-chem-phys-discuss.net/13/11597/2013/ acpd-13-11597-2013-supplement.pdf.

Title Page

Abstract | Introduction

Conclusions | References

Tables | Figures

|◄ | ►|

◄ | ►

Back | Close

Full Screen / Esc

Printer-friendly Version

Interactive Discussion

References

Andreas, E. L.: A new sea spray generation functions for wind speeds up to $32\,\mathrm{m\,s^{-1}}$, J. Phys. Oceanogr., 28, 2175–2184, 1998. 11600

Bentamy, A., Queffeulou, P., Quilfen, Y., and Katsaros, K.: Ocean surface wind fields estimated from satellite active and passive microwave instruments, IEEE Geosci. Remote S., 37, 2469–2486, 1997. 11614

Betts, A. K.: A new convective adjustment scheme, Part I: Observational and theoretical basis., Q. J. Roy. Meteor. Soc., 112, 677–691, 1986. 11603

Betts, A. K. and Miller, M. J.: A new convective adjustment scheme, Part II: Single column tests using GATE wave, BOMEX, ATEX and Artic air-mass data sets, Q. J. Roy. Meteor. Soc., 112, 693–709, 1986. 11603

Bormann, N. and Marks, C. J.: Mesoscale rainfall forecasts over New Zealand during SALPEX96: characterization and sensitivity studies, Mon. Wea. Rev., 127, 2880–2893, 1999. 11624

Caffrey, P. F., Hoppel, W. A., and Shi, J. J.: A one-dimensional sectional aerosol model integrated with mesoscale meteorological data to study marine boundary layer aerosol dynamics, J. Geophys. Res., 111, D24201, doi:10.1029/2006JD007237, 2006. 11600, 11607

Chin, M., Ginoux, P., Kinne, S., Torres, O., Holben, B. N., Duncan, B. N., Martin, R. V., Logan, J. A., Higurashi, A., and Nakajima, T.: Tropospheric aerosol optical thickness from the GO-CART model and comparisons with satellite and sun photometer measurements, J. Atmos. Sci., 59, 461–483, 2002. 11600, 11607

Clarke, A. D., Owens, S. R., and Zhou, J.: An ultrafine sea-salt flux from breaking waves: implications for cloud condensation nuclei in the remote marine atmosphere, J. Geophys. Res., 111, D06202, doi:10.1029/2005JD006565, 2006. 11600

d'Almeida, G. A.: Atmospheric Aerosolsx, Deepak Publishing, Hampton, Virginia, 561 pp., 1991. 11608

de Leeuw, G., Neele, F. P., Hill, M., Smith, M. H., and Vignati, E.: Production of sea spray aerosol in the surf zone, J. Geophys. Res., 105, 29397–29409, 2000. 11600

de Leeuw, G., Andreas, E. L., Anguelova, M. D., Fairall, C. W., Lewis, E. R., O'Dowd, C., Schulz, M., and Schwartz, S. E.: Production flux of sea spray aerosol, Rev. Geophys, 49, RG2001, doi:0.1029/2010RG000349, 2011. 11599, 11600

Modeling of the global distribution of sea-salt aerosol

M. Spada et al.

Title Page

Abstract | Introduction

Conclusions | References

Tables | Figures

|◀ | ▶|

◀ | ▶

Back | Close

Full Screen / Esc

Printer-friendly Version

Interactive Discussion

Dunbar, R., Lungu, T., Weiss, B., Stiles, B., Huddleston, J., Callahan, P. S., Shirtliffe, G., Perry, K. L., Hsu, C., Mears, C., Wentz, F., and Smith, D.: QuikSCAT Science Data Product User Manual, Version 3.0, September 2006, Tech. rep., JPL Document D-18053 – Rev A, Jet Propulsion Laboratory, Pasadena, CA., 2006. 11611

5 Fan, T. and Toon, O. B.: Modeling sea-salt aerosol in a coupled climate and sectional micro-physical model: mass, optical depth and number concentration, Atmos. Chem. Phys., 11, 4587–4610, doi:10.5194/acp-11-4587-2011, 2011. 11600, 11606, 11607, 11609, 11619

Fels, S. B. and Schwarzkopf, M. D.: The simplified exchange approximation: a new method for radiative transfer calculations, J. Atmos. Sci., 32, 1475–1488, 1975. 11603

10 Ferrier, B. S., Jin, Y., Lin, Y., Black, T., Rogers, E., and DiMego, G.: Implementation of a new frid-scale cloud and precipitation shceme in the NCEP Eta Model, in: Proc. 15th Conf. on Nu-merical Weather Prediction, San Antonio, 12–16 August 2002, TX, American Meteorological Society, 280–283, 2002. 11603, 11609

Gerber, H.: Relative-humidity parameterization of the navy aerosol model (NAM), Tech. rep.,
15 Tech. Rep. 8956, National Research Laboratory, Washington DC, 1985. 11600

Ghan, S. J., Laulainen, N., Easter, R. C., Wagener, R., Nemesure, S., Chapman, E., and Leung, Y. Z. R.: Evaluation of aerosol direct radiative forcing in MIRAGE, J. Geophys. Res., 106, 5295–5316, 2001. 11600

Gong, S. L.: A parameterization of sea-salt aerosol source function for sub and super-micron
20 particles, Global Biogeochem. Cy., 17, 1097, doi:10.1029/2003GB002079, 2003. 11600, 11606, 11614, 11638

Gong, S. L., Lavoué, D., Zhao, T. L., Huang, P., and Kaminski, J. W.: GEM-AQ/EC, an on-line global multi-scale chemical weather modelling system: model development and evaluation of global aerosol climatology, Atmos. Chem. Phys., 12, 8237–8256, doi:10.5194/acp-12-8237-
25 2012, 2012. 11601

Haustein, K., Pérez, C., Baldasano, J. M., Jorba, O., Basart, S., Miller, R. L., Janjic, Z., Black, T., Nickovic, S., Todd, M. C., Washington, R., Müller, D., Tesche, M., Weinzierl, B., Esselborn, M., and Schladitz, A.: Atmospheric dust modeling from meso to global scales with the online NMMB/BSC-Dust model – Part 2: Experimental campaigns in Northern Africa, Atmos. Chem.
30 Phys., 12, 2933-2958, doi:10.5194/acp-12-2933-2012, 2012. 11601, 11604

Holben, B. N., Eck, T. F., Slutsker, I., Tanré, D., Buis, J. P., Setzer, A., Vermote, E., Reagan, J. A., Kaufman, Y., Nakajima, T., Lavenu, F., Jankowiak, I., and Smirnov, A.: AERONET – a

Modeling of the global distribution of sea-salt aerosol

M. Spada et al.

Title Page

Abstract | Introduction

Conclusions | References

Tables | Figures

◄ | ►

Back | Close

Full Screen / Esc

Printer-friendly Version

Interactive Discussion

federated instrument network and data archive for aerosol characterization, Remote Sens. Environ., 66, 1–16, 1998. 11613

Hoppel, W. A., Frick, G. M., and Fitzgerald, J. W.: Surface source function for sea-salt aerosol and aerosol dry deposition to the ocean surface, J. Geophys. Res., 107, 4382, doi:10.1029/2001JD002014, 2002. 11600, 11606, 11622

Jaeglé, L., Quinn, P. K., Bates, T. S., Alexander, B., and Lin, J.-T.: Global distribution of sea salt aerosols: new constraints from in situ and remote sensing observations, Atmos. Chem. Phys., 11, 3137–3157, doi:10.5194/acp-11-3137-2011, 2011. 11599, 11600, 11611, 11612, 11613, 11617, 11622

Janjic, Z. I.: Pressure gradient force and advection scheme used for forecasting with steep and small scale topography, Contributes to Atmospheric Physics, 150, 186–199, 1977. 11602

Janjic, Z. I.: Forward-backward scheme modified to prevent two-grid interval noise and its application in sigma coordinate models, Contributes to Atmospheric Physics, 52, 69–84, 1979. 11602

Janjic, Z. I.: Non-linear advection schemes and energy cascade on semi-staggered grids, Mon. Wea. Rev., 112, 1234–1245, 1984. 11602

Janjic, Z. I.: The step-mountain eta coordinate model: physical package, Mon. Wea. Rev., 118, 1429–1443, 1990. 11602

Janjic, Z. I.: The step-mountain eta coordinate model: further developments of the convection, viscous sublayer, and turbulence closure schemes, Mon. Wea. Rev., 122, 927–945, 1994. 11602, 11603

Janjic, Z. I.: The surface layer in the NCEP eta model, 11th Conference on Numerical Weather Prediction, Norfolk, VA, 19–23 August 1996; American Meteorological Society, Boston, MA, 354–355, 1996. 11602, 11603

Janjic, Z. I.: Comments on "Development and evaluation of a convection scheme for use in climate models", J. Atmos. Sci., 57, 3686–3686, doi:10.1175/1520-0469(2000)057¡3686:CODAEO¿2.0.CO;2, 2000. 11603

Janjic, Z. I.: Nonsingular implementation of the Mellor-Yamada Level 2.5 Scheme in the NCEP Meso model, Tech. rep., NOAA/NWS/NCEP Office Note No. 436, 61 pp., avalaible at: http://www.emc.ncep.noaa.gov/officenotes/newernotes/on437.pdf, 2001. 11602, 11603

Janjic, Z. I.: A nonhydrostatic model based on a new approach, Meteorol. Atmos. Phys., 82, 271–285, doi:10.1007/s00703-001-0587-6, 2003. 11602

Title Page

Abstract | Introduction

Conclusions | References

Tables | Figures

|◀ | ▶|

◀ | ▶

Back | Close

Full Screen / Esc

Printer-friendly Version

Interactive Discussion

Janjic, Z. I.: A unified model approach from meso to global scales, Geophysical Research Abstracts, 7, SRef–ID: 1607–7962/gra/EGU05–A–05 582, 2005. 11601

Janjic, Z. I. and Black, T.: A unified model approach from meso to global scales, Geophysical Research Abstracts, 7, SRef–ID: 1607–7962/gra/EGU2007–A–05 025, 2007. 11601

5 Janjic, Z.: Further development of the unified multiscale Eulerian model for a broad range of spatial and temporal scales within the new National Environmental Modeling System, EGU General Assembly 2009, held 19–24 April 2009, Wien, Austria, abstract EGU2009-1587, 11, 1587 pp., 2009. 11602, 11605

Janjic, Z. I. and Gall, R.: Scientific documentation of the NCEP nonhydrostatic mul-
10 tiscale model on the B grid (NMMB), Part 1 Dynamics, Tech. rep., NCAR/TN-489+STR, doi:10.5065/D6WH2MZX, availabe at: http://nldr.library.ucar.edu/repository/collections/TECH-NOTE-000-000-000-857, 2012. 11601, 11602

Janjic, Z. I., Gerrity, J. P., and Nickovic, S.: An alternative approach to non-hydrostatic modeling, Mon. Wea. Rev., 129, 1164–1178, doi:10.1175/1520-
15 0493(2001)129<1164:AAATNM>2.0.CO;2, 2001. 11602

Janjic, Z. I., Janjic, T., and Vasic, R.: A class of conservative fourth order advection schemes and impact of enhanced formal accuracy on extended range forecasts, Mon. Wea. Rev., 139, 1556–1568, doi:10.1175/2010MWR3448.1, 2011. 11601, 11602

Jorba, O., Dabdub, D., Blaszczak-Boxe, C., Pérez, C., Janjic, Z., Baldasano, J. M., Spada,
20 M., Badia, A., and Gonçalves, M.: Potential significance of photoexcited NO_2 on global air quality with the NMMB/BSC chemical transport model, J. Geophys. Res., 117, D13301, doi:10.1029/2012JD017730, 2012. 11601, 11602, 11628

Katzfey, J. J.: Simulation of extreme New Zealand precipitation events, Part I: Sensitivity of orography and resolution, Mon. Wea. Rev., 123, 737–754, 1995a. 11624

25 Katzfey, J. J.: Simulation of extreme New Zealand precipitation events. Part II. Mechanisms of precipitation development., Mon. Wea. Rev., 123, 755–775, 1995b. 11624

Köepke, P., Hess, M., Schult, I., and Shettle, E. P.: Global aerosol dataset, report, Tech. rep., Max-Planck Institute für Meteorologie, Hamburg, Germany, 1997. 11608

Lacis, A. A. and Hansen, J. E.: A parameterization for the absorption of solar radiation in the
30 Earth's atmosphere, J. Atmos. Sci., 31, 118–133, 1974. 11603

Lewis, E. R. and Schwartz, S. E.: Sea Salt Aerosol Production: Mechanisms, Methods, Measurements, and Models, American Geophysical Union, Washington DC, 9-13, 2004. 11599, 11600, 11605, 11606, 11609, 11610

Mårtensson, E. M., Nilsson, E. D., de Leeuw, G., Cohen, L. H., and Hansson, H.-C.: Laboratory simulations and parameterization of the primary marine aerosol production, J. Geophys. Res., 108, 4297, doi:10.1029/2002JD002263, 2003. 11600, 11606, 11614, 11638

McCauley, M. P. and Sturman, A. P.: A study of orographic blocking and barrier wind development upstream of the Southern Alps, New Zealand, Meteorol. Atmos. Phys., 70, 121–131, 1999. 11623

Mellor, G. L. and Yamada, T.: Development of a turbulence closure model for geophysical fluid problems, Rev. Geophys. Space Phys., 20, 851–875, 1982. 11603

Mishchenko, M. I., Travis, L. D., and Lacis, A. A.: Scattering, Absorption, and Emission of Light by Small Particles, Cambridge University Press, Cambridge, 2002. 11609, 11610

Mlawer, E. J., Taubman, S. J., Brown, P. D., Iacono, M. J., and Clough, S. A.: Radiative transfer for inhomogeneous atmosphere: RRTM, a validated correlated-k model for the longwave, J. Geophys. Res., 102, 16663–16682, 1997. 11603

Monahan, E. C., Spiel, D. E., and Davidson, K. L.: A model of marine aerosol generation via whitecaps and wave disruption, in: Oceanic Whitecaps, edited by: Monahan, E. C. and Mac Niocaill, G., 167–174, D. Reidel, Norwell, Massachusetts, 1986. 11600, 11606, 11614, 11638

Monin, A. S. and Obukhov, A. M.: Basic laws of turbulent mixing in the surface layer of the atmosphere, Contrib. Geophys. Inst. Acad. Sci. USSR, 151, 163–187, 1954 (in Russian). 11603

O'Dowd, C. D. and de Leeuw, G.: Marine aerosol production: a review of the current knowledge, Philos. T. Roy. Soc. A, 365, 1753–1774, doi:10.1098/rsta.2007.2043, 2007. 11600, 11606

O'Neill, N., Eck, T., Smirnov, A., and Holben, B.: Spectral Deconvolution Algorithm (SDA) Technical memo. Version 4.1, Tech. rep., AERONET, 2008. 11613

Pérez, C., Haustein, K., Janjic, Z., Jorba, O., Huneeus, N., Baldasano, J. M., Black, T., Basart, S., Nickovic, S., Miller, R. L., Perlwitz, J. P., Schulz, M., and Thomson, M.: Atmospheric dust modeling from meso to global scales with the online NMMB/BSC-Dust model – Part 1: Model description, annual simulations and evaluation, Atmos. Chem. Phys., 11, 13001–13027, doi:10.5194/acp-11-13001-2011, 2011. 11601, 11602, 11603, 11604, 11608, 11614, 11628

Petelski, T., Piskozub, J., and Paplinska-Swerpel, B.: Sea spray emission from the surface of the open Baltic Sea, J. Geophys. Res., 110, C10023, doi:10.1029/2004JC002800, 2005. 11600

Modeling of the global distribution of sea-salt aerosol

M. Spada et al.

Title Page

Abstract	Introduction
Conclusions	References
Tables	Figures

|◄ | ►|

◄ | ►

Back | Close

Full Screen / Esc

Printer-friendly Version

Interactive Discussion

Quilfen, Y. and Chapron, B.: The ERS scatterometer wind measurement accuracy: evidence of seasonal and regional biases, J. Atmos. Ocean. Tech., 18, 1684–1697, 2001. 11614

Quinn, P. K. and Bates, T. S.: Regional aerosol properties: Comparisons of boundary layer measurements from ACE1, ACE2, aerosols99, INDOEX, ACE asia, TARFOX, and NEAQS, J. Geophys. Res., 110, D14 202, doi:10.1029/2004JD004755, 2005. 11612

Quinn, P. K., Coffman, D. J., Kapustin, V. N., Bates, T. S., and Covert, D. S.: Aerosol optical properties in the marine boundary layer during the First Aerosol Characterization Experiment (ACE1) and the underlying chemical and physical aerosol properties, J. Geophys. Res., 103, 16547–16563, 1998. 11612

Reid, J. S., Jonsson, H. H., Smith, M. H., and Smirnov, A.: Evolution of the vertical profile and flux of large sea-salt particles in a coastal zone, J. Geophys. Res., 34, 12039–12053, 2001. 11600

Revell, M. J., Copeland, J. H., Larsen, H. R., and Wratt, D. S.: Barrier jets around the Southern Alps of New Zealand and their potential to enhance alpine rainfall, Atmos. Res., 61, 277–298, 2002. 11624

Roe, G. H.: Orographic precipitation, Ann. Rev. Earth Planet. Sci., 33, 645–671, 2005. 11623

Sandwell, D. T. and Agreen, R. W.: Seasonal variation in wind speed and sea state from global satellite measurements, J. Geophys. Res., 89, 2041–2051, 1984. 11615

Savoie, D. L. and Prospero, J. M.: Aerosol concentration statistics for the Northern Tropical Atlantic, J. Geophys. Res., 82, 5954–5964, doi:10.1029/JC082i037p05954, 1977. 11612

Simmons, A. J. and Burridge, D. M.: An energy and angular momentum conserving vertical finite-difference scheme and hybrid vertical coordinates, Mon. Wea. Rev., 109, 758–766, 1981. 11602

Sinclair, M., Wratt, D. S., Henderson, R. D., and Gray, W. R.: Factors affecting the distribution and spillover of precipitation in the Southern Alps of New Zealand – a case study, J. Appl. Meteorol., 36, 428–442, 1997. 11623

Slinn, W. G. N.: Predictions for particle deposition to vegetative canopies, Atmos. Environ., 16, 1785–1794, 1982. 11608

Slinn, W. G. N.: Precipitation scavenging, in: Atmospheric Science and Power Production, edited by: Randerson, D., 466–532, OSTI, Oak Ridge, 1984. 11609

Smirnov, A., Holben, B. N., Eck, T. F., Dubovik, O., and Slutsker, I.: Cloud screening and quality control algorithms for the AERONET data-base, Remote Sens. Environ., 73, 337–349, doi:10.1016/S0034-4257(00)00109-7, 2000. 11613

Modeling of the global distribution of sea-salt aerosol

M. Spada et al.

Title Page

Abstract	Introduction
Conclusions	References
Tables	Figures

|◀ | ▶|

◀ | ▶

Back | Close

Full Screen / Esc

Printer-friendly Version

Interactive Discussion

Smirnov, A., Holben, B. N., Giles, D. M., Slutsker, I., O'Neill, N. T., Eck, T. F., Macke, A., Croot, P., Courcoux, Y., Sakerin, S. M., Smyth, T. J., Zielinski, T., Zibordi, G., Goes, J. I., Harvey, M. J., Quinn, P. K., Nelson, N. B., Radionov, V. F., Duarte, C. M., Losno, R., Sciare, J., Voss, K. J., Kinne, S., Nalli, N. R., Joseph, E., Krishna Moorthy, K., Covert, D. S., Gulev, S. K., Milinevsky, G., Larouche, P., Belanger, S., Horne, E., Chin, M., Remer, L. A., Kahn, R. A., Reid, J. S., Schulz, M., Heald, C. L., Zhang, J., Lapina, K., Kleidman, R. G., Griesfeller, J., Gaitley, B. J., Tan, Q., and Diehl, T. L.: Maritime aerosol network as a component of AERONET – first results and comparison with global aerosol models and satellite retrievals, Atmos. Meas. Tech., 4, 583–597, doi:10.5194/amt-4-583-2011, 2011. 11611, 11616

Smith, M. H. and Harrison, N. M.: The sea spray generation function, J. Atmos. Sci., 29, 189–190, 1998. 11600

Smith, M. H., Park, P. M., and Consterdine, I. E.: Marine aerosol concentrations and estimated fluxes over the sea, Q. J. Roy. Meteor. Soc., pp. 809–824, 1993. 11600, 11606, 11614, 11638

Textor, C., Schulz, M., Guibert, S., Kinne, S., Balkanski, Y., Bauer, S., Berntsen, T., Berglen, T., Boucher, O., Chin, M., Dentener, F., Diehl, T., Easter, R., Feichter, H., Fillmore, D., Ghan, S., Ginoux, P., Gong, S., Grini, A., Hendricks, J., Horowitz, L., Huang, P., Isaksen, I., Iversen, I., Kloster, S., Koch, D., Kirkevåg, A., Kristjansson, J. E., Krol, M., Lauer, A., Lamarque, J. F., Liu, X., Montanaro, V., Myhre, G., Penner, J., Pitari, G., Reddy, S., Seland, Ø., Stier, P., Takemura, T., and Tie, X.: Analysis and quantification of the diversities of aerosol life cycles within AeroCom, Atmos. Chem. Phys., 6, 1777–1813, doi:10.5194/acp-6-1777-2006, 2006. 11599, 11600, 11616

Textor, C., Schulz, M., Guibert, S., Kinne, S., Balkanski, Y., Bauer, S., Berntsen, T., Berglen, T., Boucher, O., Chin, M., Dentener, F., Diehl, T., Feichter, J., Fillmore, D., Ginoux, P., Gong, S., Grini, A., Hendricks, J., Horowitz, L., Huang, P., Isaksen, I. S. A., Iversen, T., Kloster, S., Koch, D., Kirkevåg, A., Kristjansson, J. E., Krol, M., Lauer, A., Lamarque, J. F., Liu, X., Montanaro, V., Myhre, G., Penner, J. E., Pitari, G., Reddy, M. S., Seland, Ø., Stier, P., Takemura, T., and Tie, X.: The effect of harmonized emissions on aerosol properties in global models – an AeroCom experiment, Atmos. Chem. Phys., 7, 4489–4501, doi:10.5194/acp-7-4489-2007, 2007. 11599

Title Page

Abstract | Introduction

Conclusions | References

Tables | Figures

|◄ | ►|

◄ | ►

Back | Close

Full Screen / Esc

Printer-friendly Version

Interactive Discussion

Tsigaridis, K., Koch, D., and Menon, S.: Uncertainties and importance of sea spray composition on aerosol direct and indirect effects, J. Geophys. Res., 118, 220–235, doi:10.1029/2012JD018165, 2013. 11599

Tsyro, S., Aas, W., Soares, J., Sofiev, M., Berge, H., and Spindler, G.: Modelling of sea salt concentrations over Europe: key uncertainties and comparison with observations, Atmos. Chem. Phys., 11, 10367–10388, doi:10.5194/acp-11-10367-2011, 2011. 11607

Vignati, E., Wilson, J., and Stier, P.: M7: a size resolved aerosol mixture module for the use in global aerosol models, J. Geophys. Res., 109, D22202, doi:10.1029/2003JD004485, 2004. 11600

Witek, M. L., Flatau, P. J., Quinn, P. K., and Westphal, D. L.: Global sea-salt modeling: results and validation against multicampaign shipboard measurements, J. Geophys. Res., 112, D08215, doi:10.1029/2006JD007779, 2007. 11617

Witek, M. L., Flatau, P. J., Teixeira, J., and Markowicz, K. M.: Numerical investigation of sea salt aerosol size bin partitioning in global transport models: implications for mass budget and optical depth, Aerosol Sci. Technol., 45, 401–414, doi:10.1080/02786826.2010.541957, 2011. 11605

Wratt, D. S., Revell, M. J., Sinclair, M. R., Gray, W. R., Henderson, R. D., and Chater, A. M.: Relationships between air mass properties and mesoscale rainfall in New Zealand's Southern Alps, Atmos. Res., 52, 261–282, 2000. 11623, 11626

Zakey, A. S., Solmon, F., and Giorgi, F.: Implementation and testing of a desert dust module in a regional climate model, Atmos. Chem. Phys., 6, 4687–4704, doi:10.5194/acp-6-4687-2006, 2006. 11609

Zhang, J. and Reid, J. S.: MODIS Aerosol product analysis for data assimilation: assessment of level 2 aerosol optical thickness retrievals, J. Geophys. Res., 111, D22207, doi:10.1029/2005JD006898, 2006. 11611

Zhang, L., Gong, S., Padro, J., and Barrie, L.: A size-segregated particle dry deposition scheme for an atmospheric aerosol module, Atmos. Environ., 35, 549–560, 2001. 11608

Title Page

Abstract | Introduction

Conclusions | References

Tables | Figures

◄ | ►►

◄ | ►

Back | Close

Full Screen / Esc

Printer-friendly Version

Interactive Discussion

Table 1. Sea-salt sections and their characteristic radii.

bin	r_d(µm)	r_d^{vm}(µm)	r_d^{eff}(µm)
1	0.10–0.18	0.14	0.14
2	0.18–0.30	0.24	0.24
3	0.30–0.60	0.43	0.45
4	0.60–1.00	0.77	0.79
5	1.00–1.80	1.32	1.36
6	1.80–3.00	2.27	2.32
7	3.00–6.00	3.98	4.13
8	6.00–15.00	7.39	8.64

Table 2. Sea-salt emission number fluxes implemented in NMMB/BSC-CTM. dF_N/dr fluxes in units $[\mathrm{m}^{-2}\,\mathrm{s}^{-1}\,\mathrm{\mu m}^{-1}]$, $dF_N/d\log(r)$ fluxes in units $[\mathrm{m}^{-2}\,\mathrm{s}^{-1}]$; r_{80} and r_d respectively stand for wet radius at RH = 80 % and dry radius in units $[\mathrm{\mu m}]$, r does not specificy the use of dry or wet radius. U_{10} in $\mathrm{m\,s}^{-1}$. SST in K units. Formul. range stands for the size-range in the original formulation of each parameterization. The assumption $r_{80} = 2r_d$ is used to merge wet and dry radius intervals. In this work, all the schemes are applied in the range $r_d \in [0.1\text{–}15]\,\mathrm{\mu m}$.

production scheme	ref.	mechanism	formul. range
$\left.\dfrac{dF_N^{(emi)}}{dr_{80}}\right\|_{G03} = 1.373 \cdot U_{10}^{3.41} \cdot r_{80}^{-A(r_{80})}(1 + 0.057 r_{80}^{3.45}) \cdot 10^{1.607\exp(-C(r_{80})^2)}$ $A = 4.7(1 + \theta r_{80})^{-0.017 r_{80}^{-1.44}}, \theta = 30, C = (0.433 - \log(r_{80}))/0.433$	Gong (2003)	bubbles, spume: unclear	$r_{80} \in [0.07\text{–}20]$
$\left.\dfrac{dF_N^{(emi)}}{dr_{80}}\right\|_{M86} = 1.373 \cdot U_{10}^{3.41} \cdot r_{80}^{-3}(1 + 0.057 r_{80}^{1.05}) \cdot 10^{1.19\exp(-B(r_{80})^2)}$ $B = (0.38 - \log(r_{80}))/0.65$	Monahan et al. (1986)	bubbles	$r_{80} \in [0.4\text{–}20]$
$\left.\dfrac{dF_N^{(emi)}}{dr_{80}}\right\|_{SM93} = \sum_{k=1,2} A_k(U_{10}) \exp\left[-f_k \ln\left(\frac{r_{80}}{r_k}\right)^2\right]$ $\log(A_1) = 0.0676 U_{10} + 2.43, \log(A_2) = 0.959 U_{10}^{1/2} - 1.476$ $r_1 = 2.1, r_2 = 9.2$	Smith et al. (1993)	bubbles, spume	$r_{80} \in [1\text{–}25]$
$\left.\dfrac{dF_N^{(emi)}}{d\log(2r_d)}\right\|_{MA03} = 3.84 \cdot 10^{-6} \cdot U_{10}^{3.41} \cdot (\alpha_j(r_d) \cdot \mathrm{SST} + \beta_j(r_d))$ $\alpha_j = \sum_{\xi=1,4} \alpha_{j,\xi}(2r_d)^\xi, \beta_j = \sum_{\xi=1,4} \beta_{j,\xi}(2r_d)^\xi$ $r_d \in (0.01, 0.0725) \rightarrow j = 1$ $r_d \in (0.0725, 0.2095) \rightarrow j = 2$ $r_d \in (0.2095, 1.4) \rightarrow j = 3$	Mårtensson et al. (2003)	bubbles (SST dependent)	$r_d \in [0.01\text{–}1.4]$ SST $\in [271\text{–}298]$
$\left.\dfrac{dF_N^{(emi)}}{dr}\right\|_{M86SM93} = \begin{cases} \max\left(\left.\dfrac{dF_N^{(emi)}}{dr}\right\|_{SM93}, \left.\dfrac{dF_N^{(emi)}}{dr}\right\|_{M86}\right) & \text{if } U_{10} \geq 9 \\ \left.\dfrac{dF_N^{(emi)}}{dr}\right\|_{M86} & \text{if } U_{10} < 9 \end{cases}$	Combined M86/SM93	bubbles, spume	
$\left.\dfrac{dF_N^{(emi)}}{dr}\right\|_{MA03M86SM93} = \begin{cases} \left.\dfrac{dF_N^{(emi)}}{dr}\right\|_{MA03} & \text{if } r_d \leq 1.4 \\ \left.\dfrac{dF_N^{(emi)}}{dr}\right\|_{M86SM93} & \text{if } r_d > 1.4 \end{cases}$	Combined M86/SM93/MA03	bubbles (SST), spume	

Table 3. Sea-salt hygroscopic growth factors $\phi = r_w/r_d$ at different ambient RH values.

RH(%)	ϕ
< 50	1.0
50–70	1.6
70–80	1.8
80–90	2.0
90–95	2.4
95–99	2.9
> 99	4.8

Modeling of the global distribution of sea-salt aerosol

M. Spada et al.

Table 4. Sea-salt solubility factors $e_{ss,k}$ for each size-bin k.

k	e_{ss}
1	0.6
2	0.6
3	0.6
4	0.3
5	0.3
6	0.1
7	0.1
8	0.1

Table 5. List of the observational sites used in this work, classified by network. The label clim stands for climatological data, while the label 2006 stands for data gathered during the year 2006.

code	database	station	lat	lon	year/clim
		AOD500 nm			
1	AERONET	Amsterdam Island	37.81° S	77.57° E	clim
2	AERONET	Ascension Island	14.41° S	7.98° W	clim
3	AERONET	Azores	38.53° N	28.63° W	clim
4	AERONET	Bermuda	32.37° N	64.70° W	clim
5	AERONET	Cape San Juan	18.38° N	65.62° W	2006/clim
6	AERONET	Ceilap-RG	51.60° S	69.32° W	2006/clim
7	AERONET	Coconut Island	21.43° N	157.79° W	clim
8	AERONET	Crozet Island	46.43° S	51.85° E	clim
9	AERONET	Dunedin	45.86° S	170.51° E	2006/clim
10	AERONET	Guam Island	13.43° N	144.80° E	2006/clim
11	AERONET	La Parguera	17.97° N	67.04° W	2006/clim
12	AERONET	Midway Island	28.21° N	177.38° W	2006/clim
13	AERONET	Nauru	0.52° S	166.92° E	2006/clim
14	AERONET	Reunion Island	20.88° S	55.48° E	clim
15	AERONET	Rottnest Island	32.00° S	115.50° E	clim
16	AERONET	Tahiti	17.58° S	149.61° W	2006/clim
		SURFACE CONCENTRATIONS			
a	U-MIAMI	Baring Head	41.28° S	174.87° E	clim
b	U-MIAMI	Bermuda	32.27° N	64.87° W	clim
c	U-MIAMI	Cape Grim	40.68° S	144.68° E	clim
d	U-MIAMI	Cape Point	34.35° S	18.48° E	clim
e	U-MIAMI	Chatam Island	34.92° S	176.50° W	clim
f	U-MIAMI	Fanning Island	3.92° N	159.33° W	clim
g	U-MIAMI	Invercargill	46.43° S	168.35° E	clim
h	U-MIAMI	King George Island	62.18° S	58.30° W	clim
i	U-MIAMI	Marion Island	46.92° S	37.75° E	clim
l	U-MIAMI	Miami	25.75° N	80.25° W	clim
m	U-MIAMI	Midway Island	28.22° N	177.35° W	clim
n	U-MIAMI	Oahu	21.33° N	157.70° W	clim
o	U-MIAMI	Palmer	64.77° S	64.05° W	clim
p	U-MIAMI	Reunion Island	21.17° S	55.83° E	clim
q	U-MIAMI	American Samoa	14.25° S	170.58° W	clim

Modeling of the global distribution of sea-salt aerosol

M. Spada et al.

Table 6. Model sea-salt totals and lifetime, depending on the emission scheme. The labels emi, drydep, and wetdep stand respectively for total accumulated emission, dry deposition, and wet deposition of sea-salt mass; wetdep frac = wetdep/(drydep + wetdep), <load> is the annual mean column mass load, and lifetime = <load>/(drydep + wetdep).

	M86/SM93	G03	M86	M86/SM93/ MA03
emi (Tg)	6048.9	8979.7	4312.9	6081.9
drydep (Tg)	3305.5	5487.3	2260.2	3306.4
wetdep (Tg)	2741.5	3490.1	2051.0	2773.3
wetdep frac	0.45	0.39	0.48	0.46
<load> (Tg)	6.6	7.9	5.9	7.6
lifetime (d)	0.40	0.32	0.50	0.46
lifetime (h)	9.6	7.7	12.0	11.0

Table 7. Model scores in simulating the coarse fraction of AOD500 nm in some selected stations, depending on the emission scheme. Statistics are calculated over the reference year 2006.

station	G03 bias	g.err	r	M86 bias	g.err	r	M86/SM93 bias	g.err	r	M86/SM93/MA03 bias	g.err	r
Dunedin (9)	+30.6 %	55.1 %	0.92	+28.7 %	54.0 %	0.92	+31.7 %	55.9 %	0.92	+23.1 %	50.1 %	0.93
Guam Island (10)	+15.0 %	39.4 %	0.67	+19.4 %	38.1 %	0.67	+19.5 %	38.2 %	0.67	+83.7 %	83.7 %	0.02
La Parguera (11)	+1.7 %	13.1 %	0.95	+1.5 %	12.1 %	0.96	+1.8	12.5 %	0.96	+36.7 %	36.7 %	0.91
Midway Island (12)	+4.9 %	18.5 %	0.65	+5.4 %	19.4 %	0.62	+5.9 %	19.5 %	0.63	+36.9 %	37.7 %	0.36
Nauru (13)	+46.8 %	74.9 %	0.86	+56.8 %	81.1 %	0.87	+56.0 %	80.7 %	0.87	+149.4 %	149.4 %	0.85
overall mean	+19.8 %	40.2 %	0.81	+22.3 %	40.9 %	0.81	+23.0 %	41.4 %	0.81	+66.0 %	71.5 %	0.61

bias stands for mean normalized bias =< (model − obs)/obs > ·100

g.err stands for mean normalized gross error =< |model − obs|/obs > ·100

$r = \text{cov}(\text{model,obs})/(\text{var}(\text{model}) \cdot \text{var}(\text{obs}))^{1/2}$
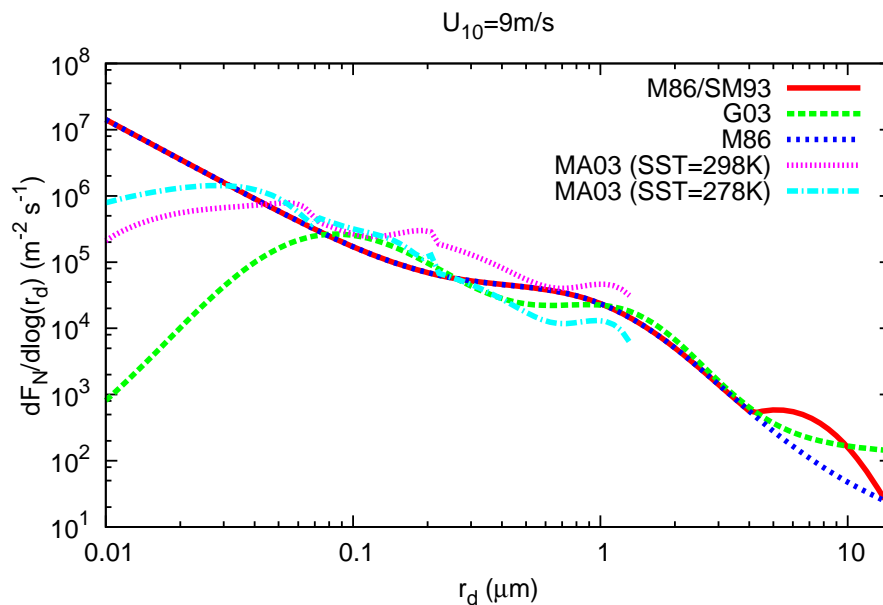
Fig. 1. Sea-salt number emission flux at 10 m wind speed of $9\,\mathrm{m\,s^{-1}}$. Parameterizations used in this work.

Title Page

Abstract | Introduction

Conclusions | References

Tables | Figures

|◄ | ►|

◄ | ►

Back | Close

Full Screen / Esc

Printer-friendly Version

Interactive Discussion
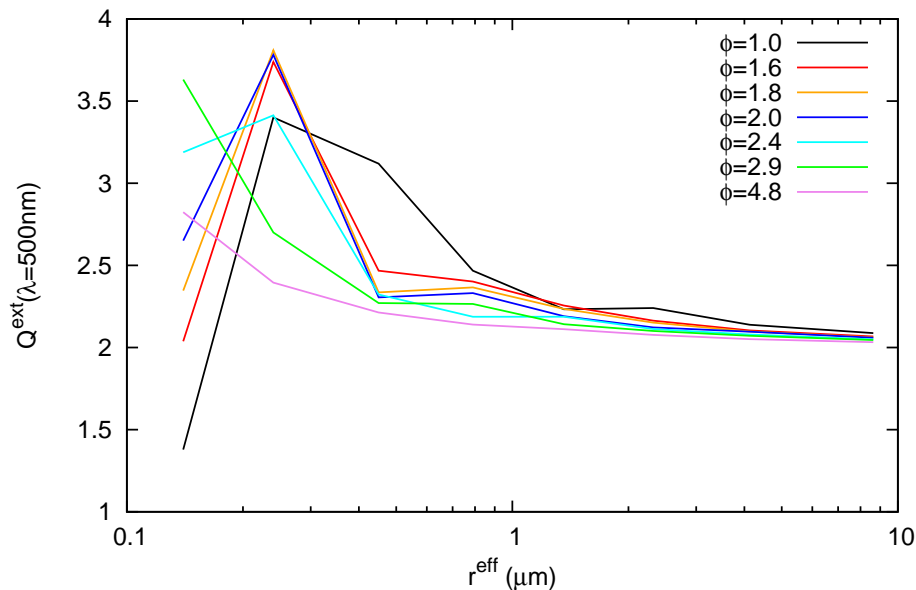
Fig. 2. Sea-salt extinction efficiency at $\lambda = 500\,\text{nm}$, depending on water-uptake growth factors ϕ of Table 3. The values are plotted as function of the effective radius of each size-bin (see Table 1).
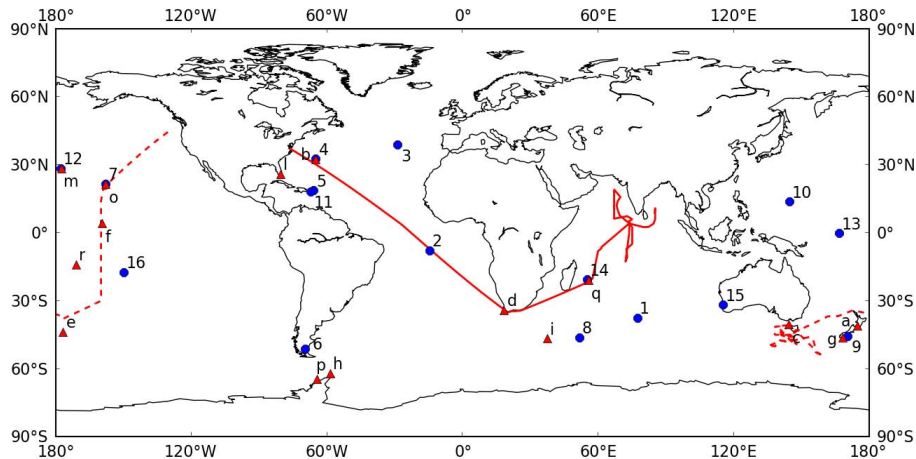
Fig. 3. Observational datasets used for the model evaluation: blue circles refer to AOD500 nm measurements from AERONET, red triangles to surface concentrations measurements from the U-MIAMI network; red lines stand for cruise measurements from AEROINDOEX (solid line), and ACE1 (dashed line).

Full Screen / Esc

Printer-friendly Version

Interactive Discussion

annual mean wind speed $(m\ s^{-1})$: NMMB(L) minus QuickSCAT

year = 2006
bias=-5.4%, g.err=6.3%
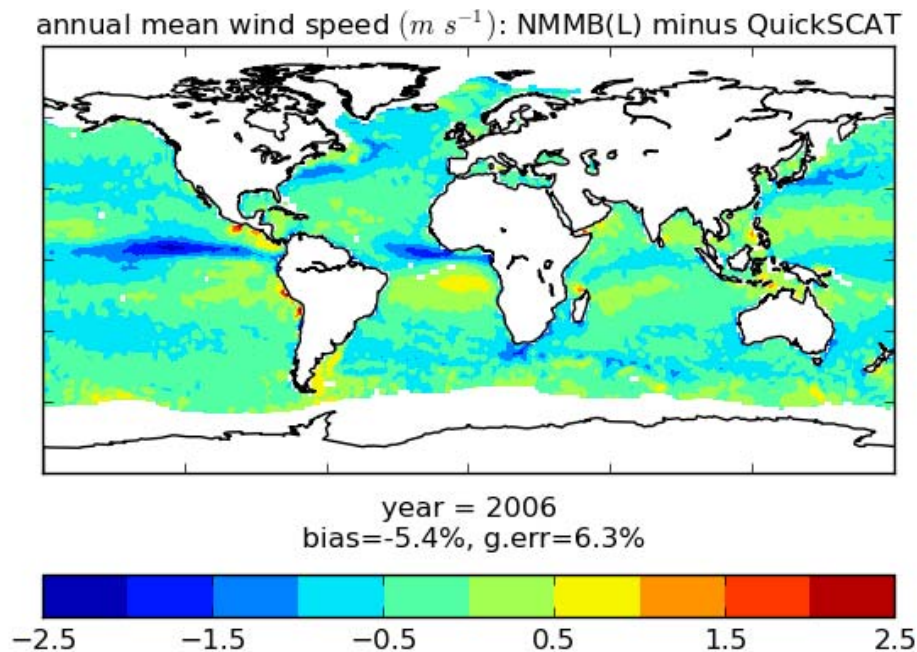
Fig. 4. Annual mean wind speed at 10 m: relative bias between NMMB at low resolution (L) and QuickSCAT satellite observations. bias =< (model−sat)/sat > ·100; g.err =< |model−sat|/sat > ·100.
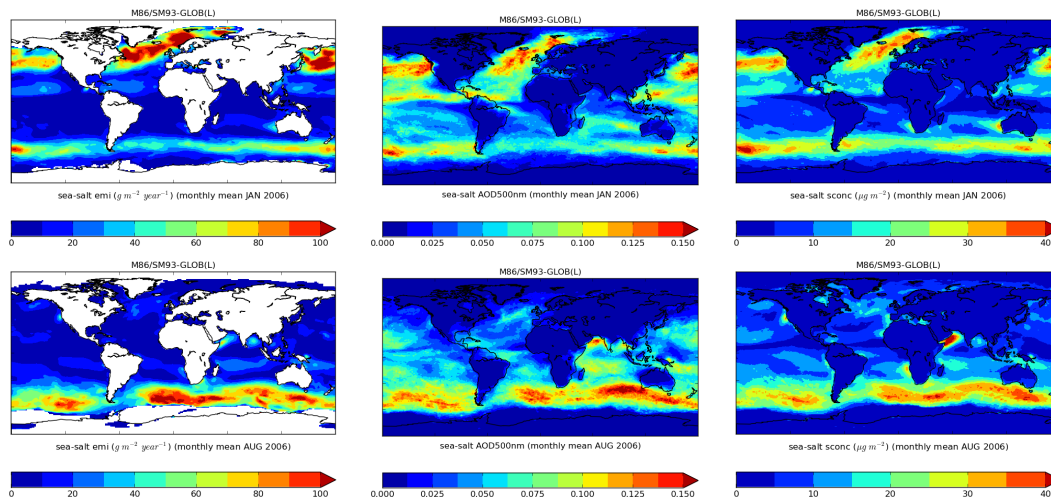
Fig. 5. Seasonal regimes of sea-salt production, surface concentrations, and AOD500 nm (January and August 2006 shown). Model maps refer to the use of M86/SM93 scheme. The label emi stands for emission flux, sconc for surface concentrations.

Fig. 6. Annual mean values of sea-salt production, surface concentrations, and AOD500 nm, depending on the emission scheme. Model maps refer to the reference year (2006). The label emi stands for emission flux, sconc for surface concentration.
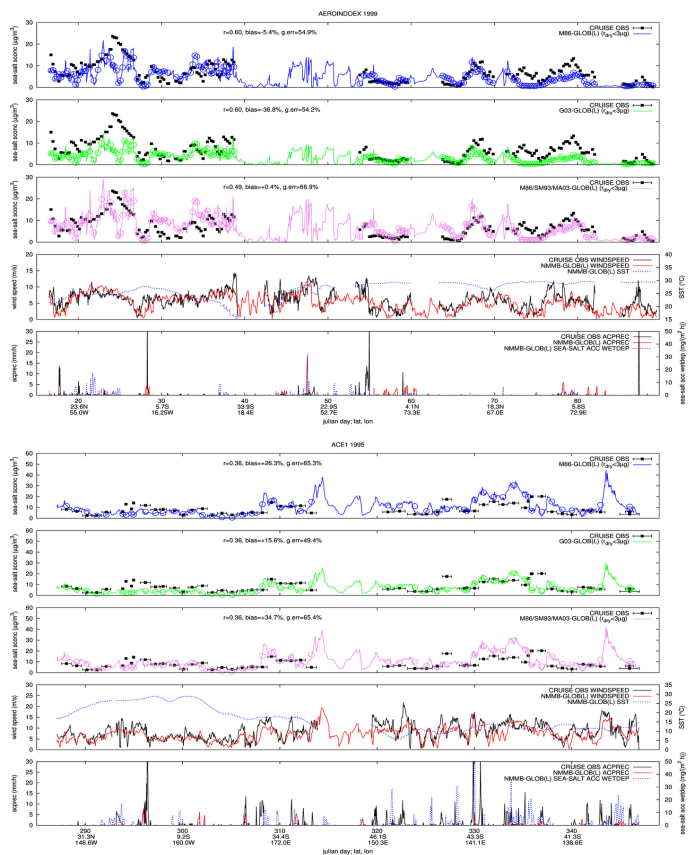
Fig. 7. Upper panels: simulated sea-salt surface concentrations (sconc) against cruise measurements. Comparison among results achieved by using respectively M86 (red), G03 (green), and M86/SM93/MA03 (violet) emission schemes; M86/SM93 is not shown since it is equivalent to M86 at the cutoff applied by measurements ($r_d < 3\,\mu m$). The measured averages are indicated with black squares, while the measurement times are shown with black bars. The model 1 h-output is plotted with solid lines and averaged over the measurement times (circles). Bottom panels: simulated wind speed and accumulated precipitations against cruise measurements (model SST and accumulated wet deposition are also shown); hourly values plotted.

Title Page

Abstract | Introduction

Conclusions | References

Tables | Figures

|◄ | ►|

◄ | ►

Back | Close

Full Screen / Esc

Printer-friendly Version

Interactive Discussion
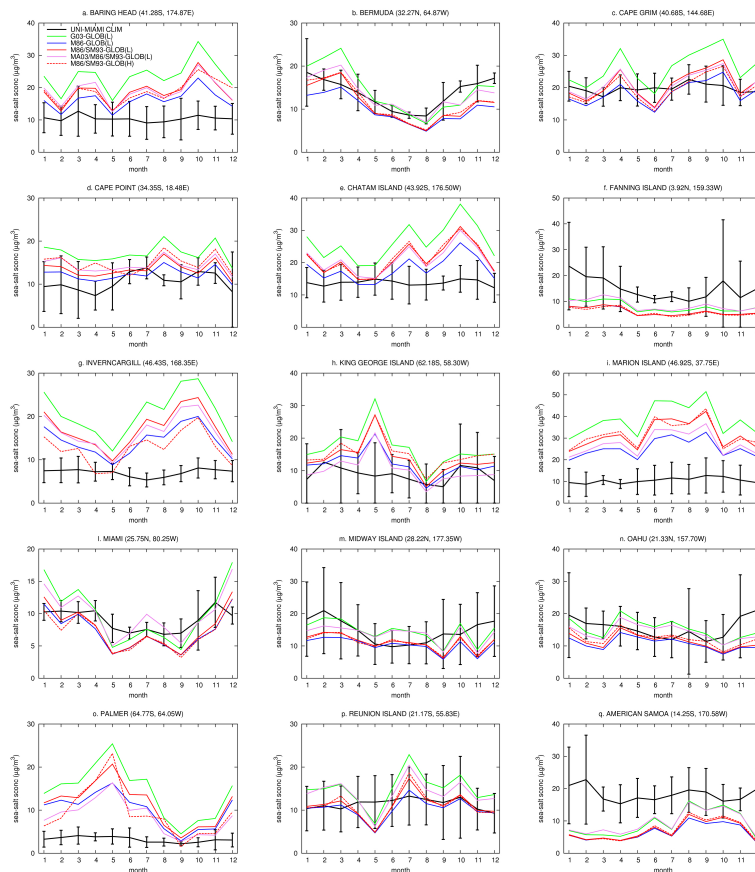
Fig. 8. Model sea-salt surface concentration monthly mean values against climatologies from U-MIAMI. Simulated values refer to the reference year (2006). The performance of the different implemented schemes is shown. The U-MIAMI climatologies are supplied of interannual standard deviation bars. The label CLIM stand for climatologies.
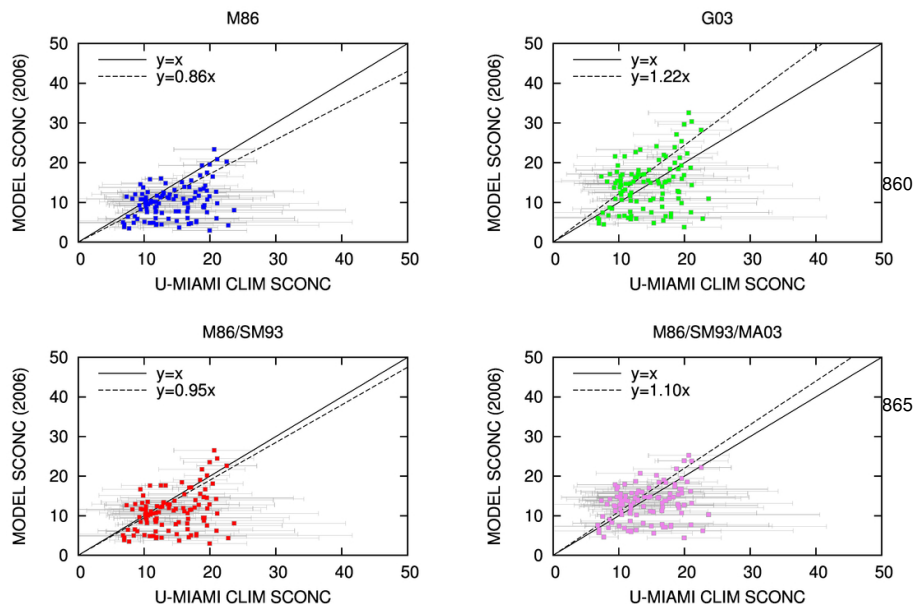
Fig. 9. Scatterplots of simulated surface monthly mean concentrations against climatologies from the U-MIAMI network, depending on the emission scheme. 9 stations used: Bermuda **(b)**, Cape Grim **(c)**, Cape Point **(d)**, Fanning Island **(f)**, Miami **(l)**, Midway Island **(m)**, Oahu **(n)**, Reunion Island **(p)**, and American Samoa **(q)**. The plots are accompanied by linear regression fits (dashed lines). The model values refer to 2006. The interannual standard deviation bars of climatologies are shown.
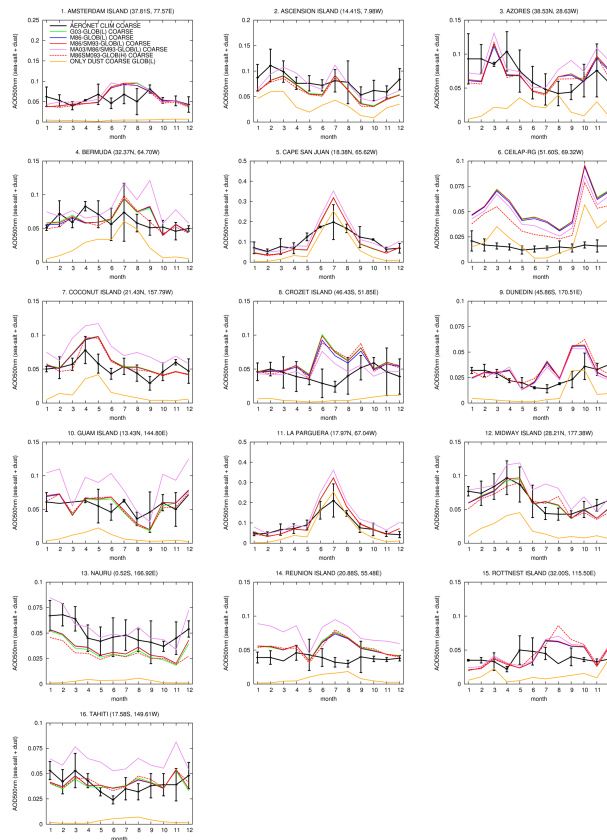
Fig. 10. Model sea-salt + dust coarse AOD500 nm monthly mean values against climatologies from AERONET. Simulated values refer to the reference year 2006. The performance of the different implemented schemes is shown. The AERONET climatologies are supplied of inter-annual standard deviation bars. The dust contribution is highlighted with the orange line. The label COARSE stands for coarse fraction of AOD; the label CLIM stand for climatologies.
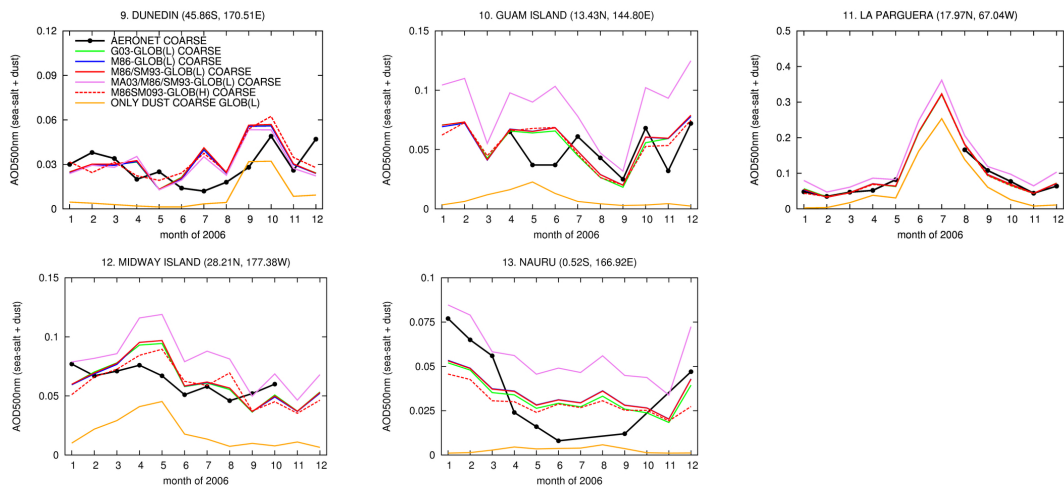
Fig. 11. Model sea-salt + dust coarse AOD500 nm monthly mean values against measurements from AERONET. Simulated and observed values refer to the same year (2006). The dust contribution is highlighted with the orange line. The label COARSE stands for coarse fraction of AOD.
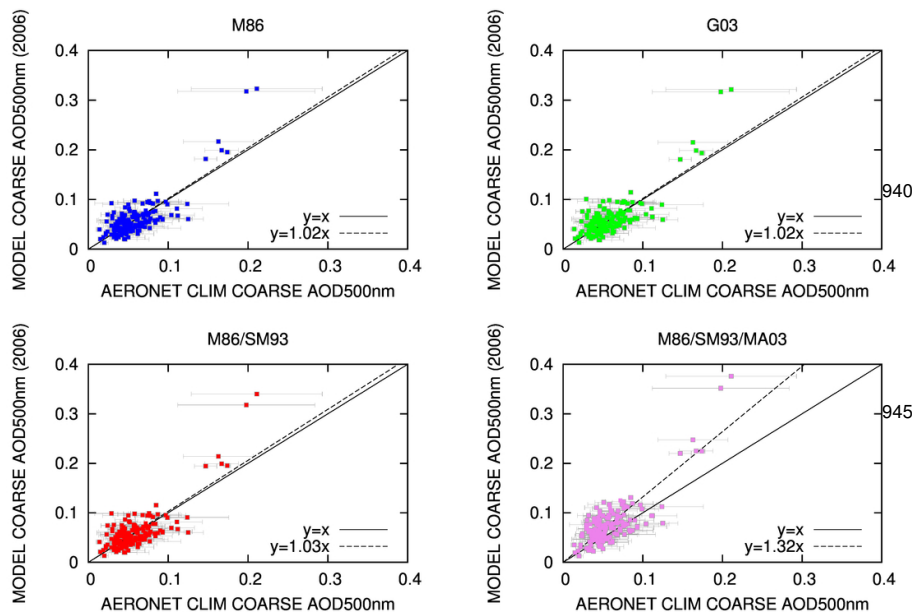
Fig. 12. Scatterplots of simulated monthly mean sea-salt + dust coarse AOD500 nm against climatologies from the AERONET network, depending on the emission scheme. 15 stations used; Ceilap-RG has been excluded, since the dust errors affecting its region. The plots are accompanied by linear regression fits (dashed lines). The model values refer to 2006. The interannual standard deviation bars of climatologies are shown.
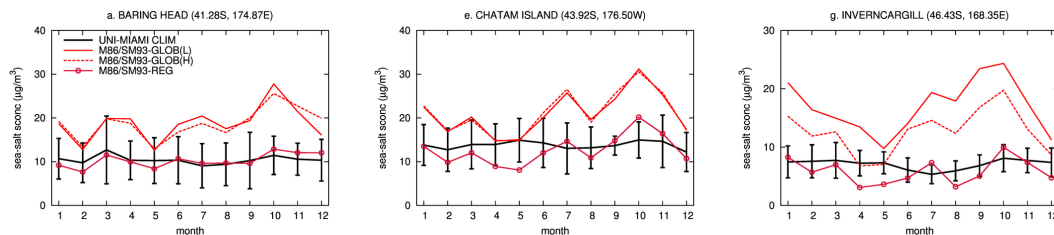
Fig. 13. Model monthly mean surface concentration values (red lines) against climatologies from the U-MIAMI (black lines). Model values refer to 2006. The label CLIM stands for climatological data. The labels REG, GLOB(L), and GLOB(H) specify the employed model resolution and domain.
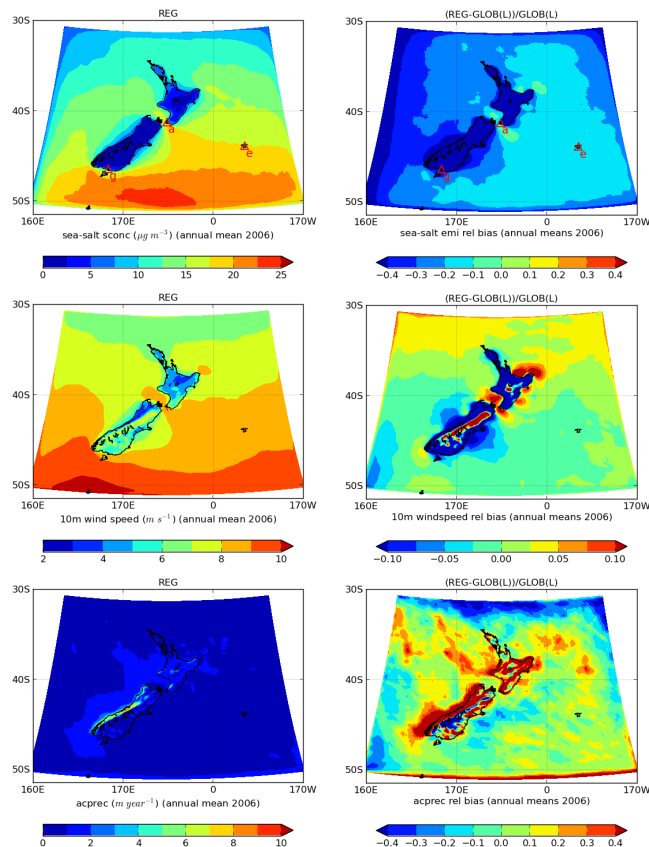
Fig. 14. On the left: annual mean surface concentrations, annual mean wind speed at 10 m, and annual accumulated precipitations as resulting from the regional simulation (REG). On the right: relative bias of annual mean surface concentrations, annual mean wind speed at 10 m, and annual accumulated precipitations between the regional simulation and the global simulation at low resolution (GLOB(L)). The GLOB(L) values have been bilinearly interpolated onto the regional grid. All the values refer to the 2006. The U-MIAMI stations of Fig. 13 have been highlighted in the concentration maps (stations are located at the center of red triangles).

Title Page

Abstract | Introduction

Conclusions | References

Tables | Figures

|◀ | ▶|

◀ | ▶

Back | Close

Full Screen / Esc

Printer-friendly Version

Interactive Discussion